Localized negative core-mantle boundary heat flux

Methods and Supplementary material

Frédéric Deschamps[1*], Joshua Martin Guerrero[1], Hagay Amit[2], Filipe Terra-Nova[3], and Wen-Pin Hsieh[1]

[1] Institute of Earth Sciences, Academia Sinica, 128 Academia Road Sec. 2, Nangang, Taipei 11529, Taiwan

[2] Laboratoire de Planétologie et Géosciences, Université de Nantes, 2, rue de la Houssinière, BP 92208, 44322 Nantes cedex 3, France

[3] Université Paris Cité, Institut de Physique du Globe de Paris, CNRS, 1 Rue Jussieu, 75005 Paris, France

*** Correspondance:** Frédéric Deschamps, frederic@earth.sinica.edu.tw

This file contains the Methods section with details on the numerical simulations, supplementary tables S1 to S3, supplementary figures S1 to S20 and a brief description of supplementary movies M1-M4.

Methods

Numerical setup

We perform numerical simulations of thermo-chemical convection with StagYY[27], solving conservation of mass, energy, momentum and composition for a compressible, infinite Prandtl number fluid. The numerical setup is very close to that used in ref. 28, with some differences, mainly the grid resolution. All simulations are run in non-dimensional units and rescaled during post-processing. Supplementary Table S1 lists the input parameters values.

Geometry and general physical properties. Conservation equations are solved on a spherical annulus[48] sampled by 256 vertical and 2048 longitudinal nodes. In addition, we prescribed grid refinement at the top and at the bottom of the annulus to describe more precisely the thermal boundary layers in these regions. The ratio between the radius of the core and the total radius is set to its Earth value, *i.e.*, $f = 0.55$. The bottom and surface boundaries are free slip and isothermal, with surface and bottom temperature fixed to 300 K and 3750 K, respectively.

A phase transition is added at a depth of 660 km, modeling the transformation of ringwoodite into bridgmanite and ferro-periclase at 660 km. For this, we define a point on the phase boundary and a Clapeyron slope, Γ_{660}. Here, we imposed d = 660 km and T = 1900 K as anchor point, and Γ_{660} = -2.5 MPa/K. Except for one case, we didn't include the phase transition to post-perovskite (pPv). In that one case, the pPv phase transition is modelled with a reference temperature of 2650 K at a depth of 2700 km depth, and lateral deviations in the transition depth are determined using the phase function approach in ref. 49. The Clapeyron slope and the density contrast are respectively set to Γ_{pPv} = 13 MPa/K[50] and $\Delta\rho_{pPv}$ = 62 kg/m^3, corresponding to a relative contrast of ~ 1.0%.

Viscosity is allowed to vary with depth, temperature, and composition. An additional viscosity ratio $\Delta\eta_{660}$ = 30 is added at the 660-km phase transition. Furthermore, to avoid the formation of stagnant lid at the top of the system, we impose a yield stress. The viscosity η is then fully described by

$$\eta = \frac{1}{\frac{1}{\eta_b}+\frac{1}{\eta_Y}}, \tag{A1}$$

where $$\eta_Y = \frac{\sigma_0+\dot{\sigma}_z P}{2\dot{e}} \tag{A2}$$

is the yield viscosity, and

$$\eta_b\left(d,T,C_{\text{prim}}\right) = \eta_0[1+29H(d-660)]exp\left[V_a\frac{d}{D}+E_a\frac{\Delta T_S}{(T+T_{off})}+K_a C_{\text{prim}}\right] \tag{A3}$$

The yield viscosity (Eq. A2) is defined from the yield stress, $\sigma_Y = \sigma_0 + \dot{\sigma}_P P$, and the second invariant of the stress tensor, $\dot{e}$. The yield stress is set to σ_0 at the surface, here equivalent to 290 MPa, and increases with pressure following a gradient (with respect to pressure) of $\dot{\sigma}_P$, here equal to 0.01. In Eq. (A3) η_0 is a reference viscosity, *H* the Heaviside step function, *d* the depth, *D* the mantle thickness, C_{prim} the concentration in dense material (see below), ΔT_S the super-adiabatic temperature difference across the system and T_{off} a temperature offset, which is added to the temperature to reduce the viscosity jump across the top thermal boundary layer and which we fixed to $T_{\text{off}} = 0.88\Delta T_S$, and. The reference viscosity η_0 is defined for the surface value of the reference adiabat (*i.e.*, $T_{as} = 0.64\Delta T_S$), and at regular composition (C_{prim} = 0). The viscosity variations with temperature are controlled by E_a, modeling the activation energy. To quantify the thermally-induced increase of viscosity, we define a potential thermal viscosity ratio as $\Delta\eta_T = \exp(E_a)$. However, due to the adiabatic increase of temperature and to the temperature offset, the effective top-to-bottom thermal viscosity contrast is smaller than $\Delta\eta_T$ by about two orders of magnitude. Here, we fixed E_a to 16.118, corresponding to $\Delta\eta_T = 10^7$, and equivalent to an activation energy of ~ 335 kJ/mol. The viscosity variations with depth are controlled by V_a, modeling the activation volume, and which we fixed to 2.303. Combined with the viscosity jump at 660 km, but excluding the decrease due to adiabatic increase of temperature and the thermally-induced increase in thermal boundary layers, this leads to a total top-to-bottom increase in viscosity by a factor 300. The viscosity variations with composition are controlled by the parameter K_a, and the viscosity ratio between primordial and regular material (or chemical viscosity ratio) is given by $\Delta\eta_C = \exp(K_a)$. In this study, we impose primordial material to be more viscous than regular material with $\Delta\eta_C$ = 30, accounting for the fact that if dense material is enriched in bridgmanite[21,51], it may be more viscous than surrounding mantle[52]. Finally, for our additional case that include the pPv phase, we assumed that pPv and bridgmanite have the same viscosity.

Because the fluid properties (density, viscosity, thermal diffusivity, and thermal expansion) are allowed to vary throughout the system, the definition of the Rayleigh number is non-unique. In our simulations, we prescribed a reference Rayleigh number Ra_0, defined at surface values of the thermodynamic parameters and reference viscosity η_0. Here, we set Ra_0 to 3.0×10^8, leading to an effective Rayleigh number (*i.e.*, the Rayleigh number at the volume average viscosity) from about 10^6 to 2.0×10^6, depending on the case. In particular, because cases we higher excess heating in piles of dense material are colder, they are slightly more viscous and have a lower Rayleigh number than other cases.

Thermochemical field. Our simulations include two types of material, modeling the regular mantle and a chemically distinct (or primordial) material, respectively. The latter accounts for chemical heterogeneities that may be present at the bottom of the mantle as a result of early differentiation, resulting in the large low shear-wave velocity provinces (LLSVPs) observed by seismic tomography maps. The compositional field is modelled with a collection of about 21 million tracers, equivalent to an average number of tracers per cell of 40, which is enough to properly model entrainment[53]. Tracers are of two types, modeling the regular mantle and primordial material, respectively, and are advected following a 4th order Runge-Kutta method. At each time step, the compositional field is inferred from the concentration C_{prim} of particles of primordial material in each cell, and varies between 0 for a cell filled with regular material only, and 1 for a cell filled with primordial material only. The primordial material is initially distributed in a basal layer. The thickness of this layer is controlled by the volume fraction of dense material, X_{prim}, which we fixed to 4 %. The primordial material is assumed to be denser than the regular (pyrolitic) mantle, and the density contrast between the two materials is controlled by the buoyancy ratio, here defined with respect to a reference density that increases with depth following a thermodynamical model of Earth's mantle,

$$B = \frac{\Delta\rho_c(d)}{\alpha_S \rho(d) \Delta T_S}, \qquad \text{(A4)}$$

where $\Delta\rho_c(d)$ is the density contrast between dense and regular material, α_S the surface thermal expansion, $\rho(d)$ the reference density at depth z, and ΔT_S the super-adiabatic temperature jump. The buoyancy ratio is fixed to $B = 0.23$, which, taking $\alpha_S = 5.0\times10^{-5}$ K^{-1}, $\rho_{bot} = 4950$ kg m^{-3}, and $\Delta T_S = 2500$ K, leads to a density contrast between dense and regular material, $\Delta\rho_C$, of 142 kg m^{-3} at the bottom of the system. For comparison, we also run a simulation with $B = 0.15$, leading to $\Delta\rho_C = 93$ kg m^{-3}.

Heat sources. The system is heated both from the bottom and from within. Compressibility generates additional sinks and sources of heat that are controlled by the dissipation number, *Di*, which varies with depth. We fixed the surface value of this number to $Di_S = 1.2$. The rates of internal heating in the regular mantle and in the primordial material are different, with primordial material assumed to have excess heating, controlled with the excess heating ratio, R_H. This difference accounts for the fact that if primordial is related to the last stages of the crystallization of magma ocean[25], it may have been enriched in heat producing elements (HPE). Estimates of excess heating ratio[37] may range between 20 and 100, depending on the assumed mantle in HPE[54,55]. The input internal heating rate, *H*, is then given by

$$H = \frac{H_{tot}}{\left[1+X_{prim}(R_H-1)\right]} \tag{A5}$$

and is chosen such that the total heating rate, H_{tot}, is equal to 11 TW, which is the median estimate of the heat generated in the mantle[36] and correspond to a surface heat flux of 21.6 mW/m^2. Here, we performed simulations for values of R_H in the range 1 (no excess heating in primordial material) to 50. To explore the upper excess heating bound for the formation of patches of negative heat flux, we further run two additional cases with $R_H = 100$. Note that because H_{tot} is fixed to the same value for all simulations, an increase in the excess heating ratio in piles of primordial material implies a decrease of the rate of heating in the regular mantle (Supplementary Figure S1).

Thermal conductivity. A key aspect of our simulations is that they account for variations of thermal conductivity with depth (pressure), temperature and composition. Supplementary Figure S2 illustrates these variations for initial profiles of temperature and composition.

Thermal conductivity of mantle mineral increase with pressure. Here, we modelled the depth-dependence with a parameterization based on experimental data for olivine[31], bridgmanite[29], and ferro-periclase[30]. In the lower mantle, this parameterization is defined assuming a mix of 80 % iron-aluminum bridgmanite and 20 % ferro-periclase along an adiabat of 300 K. Depth-dependence for each end-member is following the pressure-dependent parameterizations built in ref. 32, and by translating pressure to depth following PREM[56]. Conductivity is then obtained from geometric average of Hashin-Shtrikman upper and lower bounds[57] for such a mix. In the upper mantle, the non-dimensional conductivity is then given as a function of the non-dimensional depth by

$$\tilde{k}_d = 5.33\left(1 + 4.98\tilde{d} - 0.81\tilde{d}^2\right)/k_S \,, \tag{A6}$$

where k_S is the surface conductivity, which we here fix to 3.0 W/m/K. For the upper mantle, we build a polynomial assuming that the surface conductivity is equal, again, to 3.0 W/m/K, and that the conductivity and its derivative at a depth of 660 km-depth (corresponding to a non-dimensional depth of 0.228) are continuous with those defined for the lower mantle (Eq. A6). The resulting polynomial is given by

$$\tilde{k}_d = 3.0\left(1 + 15.66\tilde{d} - 16.38\tilde{d}^2\right)/k_S \,. \tag{A7}$$

With these parameterizations, the intrinsic (*i.e.*, excluding thermal and compositional effects) bottom to top ratio in thermal conductivity is therefore about 9.

Temperature dependence is assumed to follow a $1/T^a$ law. The reference temperature is taken at the surface, such that the non-dimensional conductivity variations with temperature is given by

$$\tilde{k}_T = \left(\frac{T_{surf}}{\Delta T \tilde{T}}\right)^a , \tag{A8}$$

where T_{surf} is the surface temperature, fixed to 300 K, ΔT_S the super-adiabatic jump, fixed to 2500 K, and $\tilde{T}$ the local non-dimensional temperature. For iron-bearing mantle material, the exponent a is expected to be around 0.5[23-24]. Slightly lower values, down to 0.2, have also been reported for various aggregate or specific minerals[33-35]. Here, we tested values of a from 0 to 1. While they may not be realistic for mantle materials, values of a lower than 0.2 or larger than 0.5 help to understand the impact of temperature-dependent thermal conductivity on the evolution of the system and on the heat flux at the CMB.

Compositional-dependence is assumed to be linear between two end-member compositions:

$$\tilde{k}_C = 1 + (R_C - 1)C_{\text{prim}} \qquad \text{(A9)}$$

where R_C is the ratio between conductivities of enriched and regular material and C_{prim} is the local fraction of dense material. The conductivity compositional-dependence is set to 1 for regular material (C_{prim} = 0). For instance, a decrease by 20 %, which may correspond to dense material enrichments of in iron by 3.0 % and in bridgmanite by 10 %[29], implies R_C = 0.8. Here, we fixed the value of R_C to 0.8 in all simulations.

For our one additional case that include the pPv phase, we assumed that the thermal conductivity of pPv is similar to that of pyrolite. Experimental results for pPv conductivity are sparse, Except for one study that report a 50 %[58] increase in pPv conductivity compared to bridgmanite, there is no experimental estimates of pPv conductivity. Importantly, in our simulations pPv is present in the form of lenses, *i.e.*, pPv does not directly sit on the CMB. Therefore, while pPv conductivity may alter the evolution of pPv lenses, it likely has a limited impact on CMB heat flux.

Finally, the non-dimensional conductivity corrected for thermal, pressure, and compositional effects is given by $\tilde{k} = \tilde{k}_d \cdot \tilde{k}_T \cdot \tilde{k}_C$, and rescaled with the surface conductivity k_S, which, again, we fixed to 3.0 W/m/K.

Simulations, post-processing and derived quantities

We performed more than 80 simulations using the setup described in the previous section. All simulations start with a transient phase during which the system is heating up. After, this phase, the flow organizes following a set of downwellings (slabs) and upwellings (plumes), and the heat transfer reach a quasi-stationary state, meaning that the top and bottom heat flux oscillates in time around nearly constant values (Supplementary Figure S3). Supplementary Tables S2 and S3 list selected output parameters (including temperature, composition and CMB heat flux statistics) averaged out in the non-dimensional time window 0.0367-0.0424, corresponding to a duration of 2 Gyr. Figures S4-S6 show snapshots of the residual temperature, composition and thermal conductivity taken at the end of simulations and representative of the thermo-chemical structures observed during the quasi-stationary phase.

Temperature, thermal conductivity and other properties are rescaled during the post-processing using the characteristic values indicated in Supplementary Table S1. Adiabatic effects on temperature are taken into account when solving the energy and momentum conservation equations, but for practical reasons, output temperature fields do not include these effects. When rescaling temperature, we and therefore corrected it for the adiabatic increase of temperature with pressure. The dimensional 'real' temperature at a given altitude z and longitude φ, $T(z, \varphi)$, is then obtained from the non-dimensional, uncompressed temperature, $\tilde{T}(z,\varphi)$, following

$$T(z,\varphi) = \left[\tilde{T}(z,\varphi) + \tilde{T}_{\text{top}}\right] a_c(z) \Delta T_S \quad \text{(A10)}$$

where $\tilde{T}_{\text{top}}$ is the surface non-dimensional temperature, here fixed to 0.12 (and which is equivalent to a dimensional surface temperature of T_{surf} = 300 K), ΔT_{S} = 2500 K is the superadiabatic temperature jump, and $a_{\text{c}}(z)$ the adiabatic correction at altitude z given by

$$a_c(z) = exp\left[\int_0^d Di_S \frac{\alpha(z)}{C_P(z)} dr\right] \quad \text{(A11)}$$

where Di_S is the surface dissipation number, $d = D - z$ is the depth (with D = 2890 km being the mantle thickness), and $\alpha(z)$ and $C_P(z)$ are the thermal expansion and heat capacity as a function of altitude. These two functions are defined as part of a reference thermodynamical model involved in the compressible form of conservation equations[59]. Practically, α decreases by a factor 5 from the surface to the core-mantle boundary (CMB), while C_P is constant with depth. The adiabatic correction defined in Eq. (A10) then varies from 1.0 at the surface to about 1.55 at the CMB.

We calculate the local CMB heat flux from the temperature distributions of our simulations using the temperature on two lowermost grid points, T_1 and T_2, plus the CMB temperature, T_{CMB}, here fixed to 3750 K. More precisely, we first estimate the temperature gradient by writing T_1 and T_2 as Taylor expansions of altitude z to the second order, and by combining these equations to cancel the second derivative of temperture. The heat flux at longitude is then given by

$$\Phi_{\mathrm{CMB}}(\varphi) = k_{\mathrm{CMB}} \frac{(r_z^2-1)T_{\mathrm{CMB}}+T_1(\varphi)-r_z^2 T_2(\varphi)}{z_1(1-r_z)} \qquad \text{(A12)}$$

where z_1 and z_2 are the altitudes of the two lowermost grid points, and $r_z = z_1/z_2$. Since T_{CMB} is fixed, the thermal conductivity on the CMB, k_{CMB}, is also constant throughout the CMB, but its value decreases with increasing temperature dependence (increasing exponent a, see previous section). Using this scheme allows, in particular, to better capture the curvature of the temperature profile in the thermal boundary layer. While our calculations are performed in a spherical annulus, we rescale the CMB power with the surface of the Earth core. In particular, the total power in the patches of negative heat flux, P_{neg}, is deduced by integrating the heat flux over the whole surface fraction S_{neg} where this flux in negative, and multiply by the core surface. Alternatively, and more straightforwardly, one may simply calculate P_{neg} from the negative patches average heat flux, $<\Phi_{neg}>$, following

$$P_{\mathrm{neg}} = 4\pi r_{CMB}^2 P_{\mathrm{neg}} \langle \Phi_{\mathrm{neg}} \rangle \qquad \text{(A13)}$$

We further defined the lateral CMB heat heterogeneity with the ratio

$$\delta\Phi = \frac{(\Phi_{\mathrm{max}} - \Phi_{\mathrm{min}})}{2\langle\Phi_{\mathrm{CMB}}\rangle}, \qquad \text{(A14)}$$

where Φ_{max}, Φ_{min} and $\langle\Phi_{\mathrm{CMB}}\rangle$ are the maximum, minimum and average heat flux, respectively. This definition is similar to that q^*, which is often used to measure heterogeneity of the CMB heat flux imposed in simulations of core dynamics, except that we set the core adiabatic heat flux, $\Phi_{\mathrm{adia}}^{\mathrm{core}}$, to zero. Here, we preferred to use $\delta\Phi$ first because it gives a more direct measure of CMB heat flux heterogeneity on the mantle side, and second because in our simulations the values of $\langle\Phi_{\mathrm{CMB}}\rangle$, which are close to or within the current estimated range of 25-110 mW/m^2 (ref. 29), are close to the estimates of $\Phi_{\mathrm{adia}}^{\mathrm{core}}$, leading to very high (and in some case negative) q^*. It should also be noted that a high $\Phi_{\mathrm{adia}}^{\mathrm{core}}$ (~ 100 mW/m^2 or more, corresponding to a power of 15 TW) would prevent the core to cool down and the geodynamo to operate.

Calculations of mean specific properties (*e.g.*, thermal conductivity or temperature) within slabs and plumes or of the altitude of piles of dense material requires to define the boundaries of these regions. Piles of dense material have very sharp boundary, meaning that the fraction of dense material at a given location, C_{prim}, decreases nearly instantaneously from 1 to 0 as the border is crossed. Here we defined the piles border with the isosurface $C_{\mathrm{prim}} = 0.9$. For the reason we just mentioned, choosing smaller values does significantly modify our results. To define the boundaries of plumes and slabs, we use a classical method based on the difference between the minimum, maximum and mean values of the temperature at a given depth[60]. Plumes and slabs are then defined as region with temperature larger (respectively, smaller) than

$$T_{\mathrm{plume}}(z) = T_{\mathrm{m}}(z) + c_{\mathrm{plume}}[T_{\mathrm{max}}(z) - T_{\mathrm{m}}(z)] \qquad \text{(A15)}$$

and $$T_{\mathrm{slab}}(z) = T_{\mathrm{m}}(z) - c_{\mathrm{slab}}[T_{\mathrm{m}}(z) - T_{\mathrm{min}}(z)] \qquad \text{(A16)}$$

with c_{plume} and c_{slab} being two constants, which we here fixed to 0.5 and 0.6, respectively.

References

48. Hernlund, J. & Tackley, P.J. Modeling mantle convection in the spherical annulus, *Phys. Earth Planet. Inter.* **171**, 48-54 (2008).

49. Christensen, U. R. & Yuen D.A. Layered convection induced by phase transitions, *J. Geophys. Res.* **90**, 10,291–10,300 (1985).

50. Tateno, S., Hirose, K., Sata, N. & Ohishi Y. Determination of post-perovskite phase transition boundary up to 4400 K and implications for thermal structure in D″ layer, *Earth Planet. Sci. Lett.* **277**, 130-136 (2009).

51. Mosca, I., Cobden, L., Deuss, A., Ritsema, J. & Trampert, J. Seismic and mineralogical structures of the lower mantle from probabilistic tomography, *J. Geophys. Res.*, **117**, B06304 (2012).

52. Yamazaki, D. & S.-I. Karato, S.-I. Some mineral physics constraints on the rheology and geothermal structure of Earth's lower mantle, *Amer. Mineralogist* **86**, 385-391 (2001).

53. Tackley, P.J. & King, S.D. Testing the tracer ratio method for modeling active compositional fields in mantle convection simulations, *Geochem. Geophys. Geosys.* **4**, 8302 (2003).

54. Arevalo, R. & McDonough, W.F. Chemical variations and regional diversity observed in MORB, *Chem. Geol.* **271**, 70–85 (2010).

55. Workman, R.K. & Hart, S.R. Major and trace element composition of the depleted MORB mantle (DMM), *Earth planet. Sci. Lett.* **231**, 53–72 (2005).

56. Dziewonski, A.M. &Anderson, D.L. Preliminary Reference Earth Model, *Phys. Earth Planet. Inter.* **25**, 297-356 (1981).

57. Hashin, Z. & Shtrikman, S. A variational approach to the theory of the effective magnetic permeability of multiphase materials, *J. Appl. Phys.*, **33**, 3125-3131 (1962).

58. Okuda, Y., Ohta, K., Hasegawa, A., Yagi, T., Hirose, K., Kawaguchi, S.I. & Ohishi, Y. Thermal conductivity of Fe-bearing post-perovskite in the Earth's lowermost mantle, *Earth Planet. Sci. Lett.*, **547**, 116466 (2020).

59. Tackley, P.J. Three-dimensional simulations of mantle convection with a thermo-chemical CMB boundary layer: D"?, in M. Gurnis et al. (eds.), The Core-Mantle Boundary Region, *Geodynamical Ser.* **28**, 231-253 (1998).

60. Labrosse, S. Hotspots, mantle plumes and core heat loss, *Earth Planet. Sci. Lett.* **199**, 147-156 (2002).

Supplementary Tables and Figures

Parameter	Symbol	Value	Units	Non-dimensional
Non-dimensional parameters				
Reference Rayleigh number	Ra_S			3.0×10^{8}
Surface dissipation number	Di_S			1.2
Total internal heating	H_{tot}	21.6	mW m^{-2}	13.454
Compositional heating ratio	R_H	1-100		
Compositional parameters				
Buoyancy ratio	B_z	142	kg m^{-3}	0.23
Volume fraction of dense material (%)	X_{prim}			4.0
Physical & thermo-dynamical parameters				
Acceleration of gravity	g	9.81	m s^{-2}	1.0
Mantle thickness	D	2891	km	1.0
Reference adiabat	T_{as}	1600	K	0.64
Super-adiabatic temperature difference	ΔT_S	2500	K	1.0
Surface density	ρ_S	3300	kg m^{-3}	1.0
Surface thermal expansion	α_S	5.0×10^{-5}	K^{-1}	1.0
Surface thermal diffusivity	κ_S	7.5×10^{-7}	m^2 s^{-1}	1.0
Heat capacity	C_P	1200	J kg^{-1} K^{-1}	1.0
Surface thermal conductivity	k_S	3.0	W m^{-1} K^{-1}	1.0
Surface Grüneisen parameter	γ_S	1.091		
Density jump at z = 660 km	$\Delta\rho_{660}$	400	kg m^{-3}	0.1212
Clapeyron slope at z = 660 km	Γ_{660}	-2.5	MPa K^{-1}	-0.0668
CMB temperature	T_{CMB}	3750	K	1.5
Density jump at CMB	$\Delta\rho_{CMB}$	5280	kg m^{-3}	1.6
Viscosity law				
Reference viscosity	η_0	1.6×10^{21}	Pa s	1.0
Viscosity ratio at z = 660 km	$\Delta\eta_{660}$	30		
Logarithmic thermal viscosity ratio	E_a	16.118		
Logarithmic vertical viscosity ratio	V_a	2.303		
Compositional viscosity ratio	$\Delta\eta_C$	32		
Surface yield stress	σ_0	290	MPa	7.5×10^{6}
Yield stress gradient	$\dot{\sigma}_z$	0.01	Pa/Pa	0.01

Table S1. Parameters and scalings of numerical simulations

a	R_H	$\langle T \rangle$ (K)	dT_{neg} (K)	dT_{pos} (K)	k_{200km} ($Wm^{-1}K^{-1}$)	$\langle T_{slab} \rangle$ (K)	V_{slab}	$\langle T_{piles} \rangle$ (K)	k_{piles} ($Wm^{-1}K^{-1}$)	h_{piles} (km)
0.00	1	2055.2	519.3	285.0	23.93	2537.6	0.137	3354.5	21.01	553.9
0.00	10	1955.0	458.7	347.8	24.34	2577.4	0.135	3386.6	20.82	704.2
0.00	15	1926.0	388.4	308.4	23.86	2700.9	0.134	3371.1	20.93	704.8
0.00	30	1859.3	502.3	384.4	24.38	2498.2	0.150	3378.9	20.73	785.5
0.00	50	1799.1	478.9	289.5	23.62	2518.3	0.114	3334.9	21.07	616.8
0.10	1	2038.2	501.5	298.4	18.86	2547.9	0.146	3335.7	16.52	568.8
0.10	10	1921.3	581.7	387.5	19.13	2405.8	0.148	3409.6	16.39	640.4
0.10	15	1885.4	592.2	411.6	19.05	2423.7	0.181	3429.8	16.39	656.5
0.10	20	1897.4	563.0	357.9	18.95	2466.9	0.151	3393.4	16.45	608.5
0.10	30	1806.0	520.8	364.9	18.93	2493.2	0.153	3390.4	16.43	675.0
0.10	50	1765.0	521.0	355.7	18.82	2403.1	0.125	3345.8	16.47	728.1
0.15	10	1925.3	538.0	409.5	17.04	2447.3	0.160	3409.9	14.47	693.3
0.15	15	1906.7	561.3	364.7	16.90	2481.9	0.166	3400.2	14.54	651.9
0.15	20	1813.8	564.6	428.8	17.06	2453.9	0.185	3436.8	14.45	702.2
0.15	30	1802.5	546.1	399.6	16.96	2482.3	0.187	3365.9	14.53	698.6
0.15	40	1793.0	583.4	403.1	16.99	2390.6	0.161	3371.7	14.53	677.6
0.15	50	1749.5	511.6	380.9	16.80	2474.4	0.170	3320.2	14.62	685.7
0.20	1	2078.2	534.7	326.6	15.06	2435.0	0.140	3315.8	12.94	630.7
0.20	5	1932.7	486.7	308.8	14.72	2568.3	0.144	3359.5	13.00	571.8
0.20	10	1931.8	580.3	403.9	15.06	2413.9	0.161	3415.8	12.86	629.5
0.20	15	1852.5	553.4	422.7	15.14	2382.4	0.146	3407.5	12.82	729.7
0.20	20	1853.4	639.8	435.7	15.13	2381.5	0.192	3439.0	12.84	632.4
0.20	30	1821.5	646.8	454.0	15.20	2350.1	0.195	3424.8	12.82	629.1
0.20	40	1789.1	571.1	423.9	15.13	2395.8	0.179	3365.6	12.87	701.6
0.20	50	1777.4	556.4	355.4	14.85	2450.6	0.167	3349.9	12.97	637.8
0.30	1	2025.1	446.2	278.3	11.58	2512.3	0.112	3317.1	10.26	578.2
0.30	5	1956.3	631.7	396.3	11.91	2391.6	0.189	3396.2	10.12	572.9
0.30	10	1926.2	656.0	440.2	11.97	2297.5	0.166	3447.4	10.06	602.4
0.30	15	1874.0	616.9	481.3	12.07	2333.1	0.171	3470.4	10.00	663.1
0.30	20	1804.0	588.5	437.5	11.87	2326.8	0.143	3441.1	10.08	672.0
0.30	30	1735.2	569.3	426.1	11.89	2375.4	0.165	3379.1	10.13	687.8
0.30	40	1772.2	664.6	497.4	12.11	2302.4	0.205	3433.5	10.04	638.2
0.30	50	1759.0	631.1	502.0	12.19	2318.5	0.207	3417.7	10.00	727.4
0.30	80	1752.4	557.8	512.3	12.36	2279.6	0.161	3365.2	9.96	774.7
0.30	100	1713.0	581.0	452.2	12.17	2291.4	0.160	3296.8	10.13	685.8

Table S2. Thermal and compositional output parameters averaged out over the last 2 Gyr of the simulations. Listed parameters are the average temperature, $\langle T \rangle$, *rms* positive and negative temperature anomalies in the bottom 200 km, dT_{neg} and dT_{pos}, average thermal conductivity in the bottom 200 km, k_{200km}, slabs average temperature and volume fraction in the bottom 200 km, $\langle T_{slab} \rangle$ and V_{slab}, and the thermo-chemical piles average temperature, $\langle T_{piles} \rangle$, thermal conductivity, k_{piles}, and maximum altitude, h_{piles}.

a	R_H	$\langle T\rangle$ (K)	dT_{neg} (K)	dT_{pos} (K)	k_{200km} ($Wm^{-1}K^{-1}$)	$\langle T_{slab}\rangle$ (K)	V_{slab}	$\langle T_{piles}\rangle$ (K)	k_{piles} ($Wm^{-1}K^{-1}$)	h_{piles} (km)
0.35	3	2034.2	614.9	413.0	10.68	2367.5	0.189	3384.5	8.94	669.2
0.35	4	1986.4	590.2	408.9	10.62	2360.3	0.164	3403.4	8.94	652.9
0.35	5	1999.1	586.7	401.8	10.62	2387.0	0.159	3404.8	8.93	650.1
0.35	10	1927.7	688.2	453.3	10.64	2269.6	0.181	3449.9	8.92	618.3
0.40	1	2051.9	613.5	325.6	9.33	2401.0	0.164	3314.5	8.05	589.6
0.40	3	2031.7	652.8	381.4	9.41	2313.4	0.159	3372.0	7.98	591.0
0.40	4	2011.4	657.5	384.8	9.38	2338.4	0.174	3391.3	7.97	585.7
0.40	5	1990.6	638.3	394.9	9.39	2354.3	0.170	3410.5	7.94	618.1
0.40	10	1936.7	628.5	492.8	9.56	2270.1	0.160	3504.2	7.78	768.4
0.40	15	1868.3	606.7	554.7	9.68	2263.5	0.160	3498.7	7.77	725.6
0.40	20	1838.1	645.5	496.6	9.54	2284.8	0.176	3481.0	7.82	717.8
0.40	30	1795.9	603.9	506.1	9.59	2317.6	0.170	3462.1	7.81	711.5
0.40	50	1735.5	700.9	547.3	9.72	2207.5	0.214	3448.7	7.83	686.9
0.50	1	2094.9	631.3	334.6	7.40	2363.5	0.176	3319.4	6.33	559.1
0.50	2	2018.9	615.0	308.1	7.23	2334.0	0.131	3356.6	6.33	545.6
0.50	3	2020.4	669.9	371.8	7.40	2337.3	0.182	3372.5	6.28	555.6
0.50	4	2020.6	640.1	386.9	7.38	2335.8	0.160	3408.2	6.24	626.8
0.50	5	1990.8	710.6	459.0	7.52	2299.8	0.215	3459.6	6.17	647.4
0.50	10	1943.1	711.0	520.6	7.57	2242.9	0.190	3534.6	6.09	687.2
0.50	15	1866.1	684.2	566.6	7.63	2281.5	0.216	3550.4	6.06	702.3
0.50	20	1823.3	778.9	564.2	7.62	2223.0	0.236	3549.7	6.08	647.4
0.50	30	1734.9	637.1	579.5	7.66	2266.8	0.203	3516.8	6.07	816.8
0.50	50	1709.4	656.1	607.2	7.77	2207.7	0.201	3498.7	6.07	791.2
0.50	100	1684.0	650.4	499.0	7.66	2265.2	0.221	3348.8	6.26	680.8
0.60	1	2068.8	581.1	362.0	5.90	2356.7	0.168	3333.1	4.96	597.3
0.60	2	2051.1	659.5	407.0	5.96	2248.5	0.157	3381.1	4.90	628.6
0.60	3	2032.8	614.4	358.3	5.79	2356.4	0.148	3384.0	4.93	577.4
0.60	4	2031.7	720.4	464.8	5.98	2229.0	0.177	3453.0	4.84	632.8
0.60	5	2006.4	734.9	471.0	5.95	2233.8	0.188	3474.4	4.83	572.7
0.60	10	1912.9	726.7	592.9	6.09	2202.1	0.207	3584.4	4.71	705.2
0.60	15	1885.9	771.0	608.3	6.06	2186.3	0.213	3613.6	4.70	650.6
0.60	20	1829.3	775.2	627.7	6.12	2125.4	0.201	3600.6	4.70	683.1
0.60	30	1777.7	739.4	545.3	5.92	2242.9	0.205	3550.1	4.78	678.2
0.60	50	1741.6	736.4	609.7	6.14	2180.2	0.222	3540.4	4.74	669.2

Table S2, continued.

a	R_H	$\langle T \rangle$ (K)	dT_{neg} (K)	dT_{pos} (K)	k_{200km} ($Wm^{-1}K^{-1}$)	$\langle T_{slab} \rangle$ (K)	V_{slab}	$\langle T_{piles} \rangle$ (K)	k_{piles} ($Wm^{-1}K^{-1}$)	h_{piles} (km)
0.80	1	2109.7	688.3	335.3	3.67	2261.0	0.155	3326.6	3.09	508.5
0.80	2	2080.0	670.1	394.7	3.69	2320.8	0.179	3409.0	3.01	601.2
0.80	3	2095.2	683.8	598.3	3.87	2242.3	0.218	3591.6	2.86	664.6
0.80	5	2049.5	778.8	608.5	3.83	2211.1	0.210	3668.6	2.83	690.2
0.80	10	1955.3	831.3	710.7	3.87	2179.5	0.256	3825.9	2.73	840.0
0.80	15	1906.4	830.1	747.2	3.84	2218.3	0.256	3859.1	2.71	735.5
0.80	20	1829.7	905.8	687.4	3.83	2179.7	0.263	3742.7	2.79	646.1
0.80	30	1786.8	859.5	735.2	3.94	2131.3	0.275	3774.7	2.76	877.0
0.80	50	1753.2	831.2	743.7	3.95	2094.1	0.238	3720.9	2.79	731.0
1.00	1	2158.9	748.6	344.1	2.31	2176.9	0.130	3351.4	1.90	481.4
1.00	2	2153.8	750.7	593.2	2.44	2199.4	0.196	3632.3	1.73	643.9
1.00	10	2032.4	761.7	874.1	2.57	2153.5	0.241	4122.7	1.52	1386.0
1.00	15	1956.0	815.6	793.4	2.51	2144.4	0.254	4004.9	1.57	1480.3
1.00	20	1913.7	764.5	956.9	2.68	2115.0	0.291	4082.6	1.50	1654.8
1.00	30	1885.8	788.2	897.0	2.69	2010.6	0.249	3826.9	1.66	1209.9
1.00	50	1820.4	672.5	1037.0	2.81	1949.8	0.204	4053.9	1.53	1284.9
					Purely thermal case					
0.50	-	2269.6	299.4	317.3	8.71	2349.2	0.092	-	-	-
					$B = 0.15$					
0.50	10	2021.7	453.5	670.0	8.17	2296.7	0.147	3529.7	5.94	1094.9
					Post-perovskite case					
0.50	10	2073.7	299.0	289.9	7.36	3075.4	0.148	3689.9	5.88	817.9

Table S2, continued.

a	R_H	$<\Phi>$ (mW m^{-2})	Φ_{min} (mW m^{-2})	Φ_{max} (mW m^{-2})	$\delta\Phi$	S_{neg}	$<\Phi_{neg}>$ (mW m^{-2})	P_{neg} (TW)	S_{sub}	$<\Phi_{sub}>$ (mW m^{-2})
0.00	1	139.4	24.5	514.1	1.76	-	-	-	0.549	42.1
0.00	10	137.6	10.6	461.3	1.64	-	-	-	0.491	26.4
0.00	15	121.5	8.3	387.6	1.56	-	-	-	0.455	29.6
0.00	30	150.1	4.8	509.8	1.67	-	-	-	0.459	24.5
0.00	50	131.3	18.1	489.2	1.80	-	-	-	0.487	39.7
0.10	1	113.8	19.4	407.0	1.70	-	-	-	0.566	35.4
0.10	10	122.3	6.0	456.9	1.85	-	-	-	0.540	19.7
0.10	15	127.4	3.1	453.4	1.77	-	-	-	0.534	18.8
0.10	20	115.1	5.0	425.8	1.83	-	-	-	0.563	21.3
0.10	30	112.9	3.6	406.5	1.79	-	-	-	0.522	22.5
0.10	50	115.6	7.8	443.5	1.89	-	-	-	0.512	28.7
0.15	10	110.8	0.1	394.2	1.78	-	-	-	0.522	16.6
0.15	15	104.1	0.5	378.2	1.81	-	-	-	0.571	18.7
0.15	20	111.2	-4.0	382.0	1.74	0.093	-2.5	-0.038	0.526	15.5
0.15	30	112.7	-3.2	375.7	1.68	0.053	-2.2	-0.022	0.535	22.1
0.15	40	114.8	2.8	409.2	1.77	-	-	-	0.547	21.6
0.15	50	111.2	6.3	370.8	1.64	-	-	-	0.511	26.4
0.20	1	102.4	15.7	378.4	1.77	-	-	-	0.576	28.6
0.20	5	82.6	10.5	308.7	1.81	-	-	-	0.605	26.5
0.20	10	97.9	0.5	372.3	1.90	-	-	-	0.556	15.6
0.20	15	99.6	-6.5	375.0	1.92	0.093	-4.3	-0.062	0.534	14.9
0.20	20	104.6	-1.9	380.8	1.83	0.057	-1.1	-0.011	0.566	11.7
0.20	30	109.8	-1.0	390.7	1.79	0.030	-0.7	-0.006	0.553	12.3
0.20	40	103.4	-1.6	363.3	1.76	0.034	-1. 1	-0.007	0.536	17.9
0.20	50	93.5	4.5	342.2	1.81	-	-	-	0.593	24.7
0.30	1	66.6	10.9	252.2	1.81	-	-	-	0.661	30.3
0.30	5	84.7	5.8	313.9	1.82	-	-	-	0.603	15.6
0.30	10	84.0	-2.8	339.5	2.04	0.13166	-1.5	-0.030	0.581	9.0
0.30	15	85.5	-11.6	320.6	1.94	0.21128	-5.6	-0.180	0.550	7.0
0.30	20	75.5	-7.8	314.8	2.14	0.18407	-3.9	-0.108	0.586	12.1
0.30	30	78.8	-5.8	294.3	1.91	0.14314	-3.2	-0.069	0.589	16.3
0.30	40	92.6	-3.4	324.4	1.77	0.16247	-1.8	-0.045	0.557	8.8
0.30	50	93.8	-5.6	315.1	1.71	0.12405	-3.4	-0.066	0.533	9.9
0.30	80	95.5	-2.4	320.5	1.62	0.10017	-1.5	-0.022	0.472	11.4
0.30	100	93.0	5.5	314.0	1.66	-	-	-	0.536	18.2

Table S3. CMB heat flux parameters over the last 2 Gyr of the simulations. Listed parameters are the average, minimum and maximum heat flux CMB , $<\Phi>$, Φ_{min} and Φ_{max}, the heat flux heterogeneity, $\delta\Phi$, the fraction of CMB area with negative heat flux, S_{neg} (dash symbol indicate that patches of negative heat flux are not observed), the average negative heat flux and total power in negative patches, $<\Phi_{neg}>$ and P_{neg}, CMB area fraction with subadiabtic heat flux (assuming Φ_{adia}^{core} = 70 mW/m^2), S_{sub}, and the average heat flux in 'subadiabtic' regions, $<\Phi_{sub}>$.

a	R_H	$\langle\Phi\rangle$ (mW m^{-2})	Φ_{min} (mW m^{-2})	Φ_{max} (mW m^{-2})	$\delta\Phi$	S_{neg}	$\langle\Phi_{neg}\rangle$ (mW m^{-2})	P_{neg} (TW)	S_{sub}	$\langle\Phi_{sub}\rangle$ (mW m^{-2})
0.35	3	81.9	3.8	305.3	1.84	-	-	-	0.591	15.3
0.35	4	75.8	1.2	293.3	1.93	-	-	-	0.603	16.2
0.35	5	73.6	-1.7	285.1	1.95	0.061	-1.1	-0.011	0.591	13.1
0.35	10	77.2	-5.2	315.8	2.08	0.147	-2.6	-0.060	0.597	7.5
0.40	1	68.7	11.5	268.4	1.87	-	-	-	0.665	21.2
0.40	3	70.3	4.2	291.6	2.04	-	-	-	0.634	15.2
0.40	4	68.5	1.4	276.3	2.01	-	-	-	0.638	13.7
0.40	5	66.2	-1.5	269.3	2.05	0.050	-0.9	-0.008	0.641	13.2
0.40	10	69.3	-15.9	286.1	2.19	0.223	-9.0	-0.301	0.587	8.3
0.40	15	72.3	-15.5	278.4	2.03	0.324	-7.7	-0.380	0.542	5.3
0.40	20	68.0	-17.3	271.1	2.12	0.222	-9.2	-0.306	0.588	6.9
0.40	30	66.6	-13.3	248.3	1.97	0.275	-7.2	-0.300	0.561	6.3
0.40	50	80.1	-9.3	287.3	1.85	0.249	-4.8	-0.180	0.563	7.4
0.50	1	57.6	8.1	229.2	1.92	-	-	-	0.687	18.0
0.50	2	46.8	5.9	226.1	2.36	-	-	-	0.768	19.4
0.50	3	55.3	3.1	232.6	2.07	-	-	-	0.677	13.2
0.50	4	51.9	-2.7	226.7	2.21	0.091	-1.7	-0.024	0.696	13.6
0.50	5	59.5	-6.5	238.3	2.06	0.154	-3.9	-0.092	0.644	8.5
0.50	10	57.7	-16.0	248.4	2.29	0.313	-7.4	-0.352	0.621	4.6
0.50	15	58.1	-16.1	227.5	2.10	0.395	-8.2	-0.494	0.585	1.7
0.50	20	61.4	-14.1	241.7	2.08	0.416	-7.7	-0.485	0.612	1.1
0.50	30	57.0	-21.7	215.9	2.09	0.281	-9.8	-0.418	0.611	8.7
0.50	50	62.6	-15.9	227.7	1.95	0.286	-8.0	-0.349	0.561	5.9
0.50	100	62.5	-3.4	214.0	1.74	0.112	-2.2	-0.039	0.622	14.5
0.60	1	44.9	4.2	182.3	2.00	-	-	-	0.729	17.7
0.60	2	48.2	0.4	213.2	2.20	-	-	-	0.694	13.9
0.60	3	38.5	-2.2	180.1	2.38	0.095	-14	-0.023	0.765	14.8
0.60	4	49.7	-6.0	216.1	2.24	0.146	-3.9	-0.086	0.668	9.1
0.60	5	47.5	-5.7	213.6	2.31	0.245	-3.3	-0.124	0.674	7.6
0.60	10	49.2	-15.6	207.6	2.27	0.410	-7.5	-0.465	0.623	3.9
0.60	15	47.6	-19.4	207.0	2.38	0.449	-9.4	-0.642	0.634	1.6
0.60	20	49.5	-19.3	214.2	2.37	0.424	-9.2	-0.595	0.620	1.8
0.60	30	40.7	-21. 6	189.7	2.60	0.380	-9.3	-0.537	0.704	5.6
0.60	50	49.4	-15.2	192.9	2.11	0.406	-7.5	-0.461	0.618	4.1

Table S3, continued.

a	R_H	$\langle\Phi\rangle$ (mW m^{-2})	Φ_{min} (mW m^{-2})	Φ_{max} (mW m^{-2})	$\delta\Phi$	S_{neg}	$\langle\Phi_{neg}\rangle$ (mW m^{-2})	P_{neg} (TW)	S_{sub}	$\langle\Phi_{sub}\rangle$ (mW m^{-2})
0.80	1	29.9	2.9	145.7	2.39	-	-	-	0.823	14.1
0.80	2	28.5	-2.1	133.8	2.38	0.146	-1.4	-0.032	0.826	13.8
0.80	3	35.4	-8.2	147.3	2.21	0.318	-5.2	-0.250	0.735	12.6
0.80	5	33.3	-13.3	154.1	2.52	0.393	-6.7	-0.399	0.742	8.5
0.80	10	33.4	-23.1	151.6	2.62	0.468	-10.0	-0.714	0.714	5.2
0.80	15	30.5	-24.6	139.1	2.70	0.465	-12.2	-0.865	0.733	5.1
0.80	20	30.7	-19.6	144.7	2.70	0.509	-10.9	-0.844	0.724	2.3
0.80	30	34.7	-20.4	148.0	2.44	0.439	-10.7	-0.715	0.695	3.8
0.80	50	33.5	-20.0	144.9	2.46	0.450	-10.1	-0.691	0.732	8.2
1.00	1	20.3	0.8	117.3	2.90	-	-	-	0.904	12.8
1.00	2	23.9	-5.8	114.8	2.53	0.352	-3.8	-0.203	0.891	16.0
1.00	10	26.0	-20.1	114.1	2.62	0.378	-9.8	-0.567	0.845	14.8
1.00	15	20.5	-17.8	106.4	3.05	0.439	-9.9	-0.664	0.885	12.1
1.00	20	27.7	-17.3	103.2	2.19	0.394	-10.6	-0.638	0.847	17.5
1.00	30	27.9	-18.6	122.5	2.55	0.412	-9.3	-0.583	0.835	15.8
1.00	50	30.5	-17.3	114.8	2.17	0.322	-9.9	-0.489	0.877	22.2
Purely thermal case										
0.50	-	100.0	4.8	258.3	1.27	-	-	-	0.276	44.0
$B = 0.15$										
0.50	10	77.2	-18.7	233.4	1.63	0.211	-11.5	-0.369	0.425	13.1
Post-perovskite case										
0.50	10	76.8	-23.0	284.85	2.01	0.394	-12.1	-0.722	0.478	-4.3

Table S3, continued.

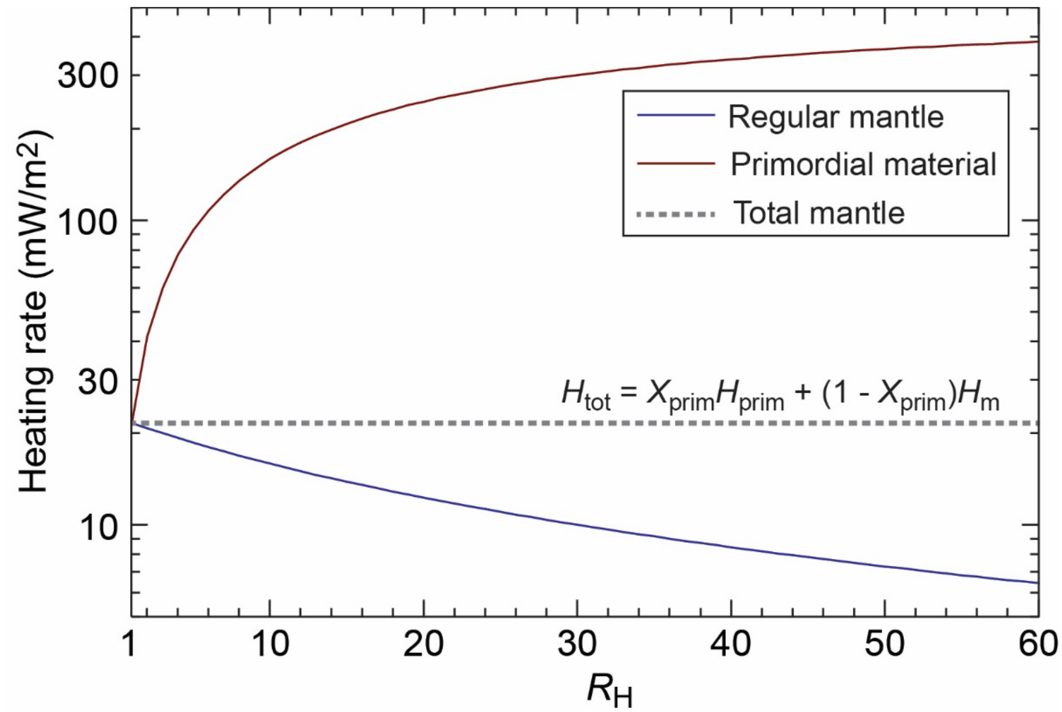

Figure S1. Internal heating rate in the regular mantle, H_m, and in the primordial material, H_{prim}, as a function of the excess heating ratio in primordial material, R_H, and for a total heating rate H_{tot} equivalent to surface heat flux of 21.6 mW/m^2 and a volume fraction of primordial material X_{prim} equal to 4 %.

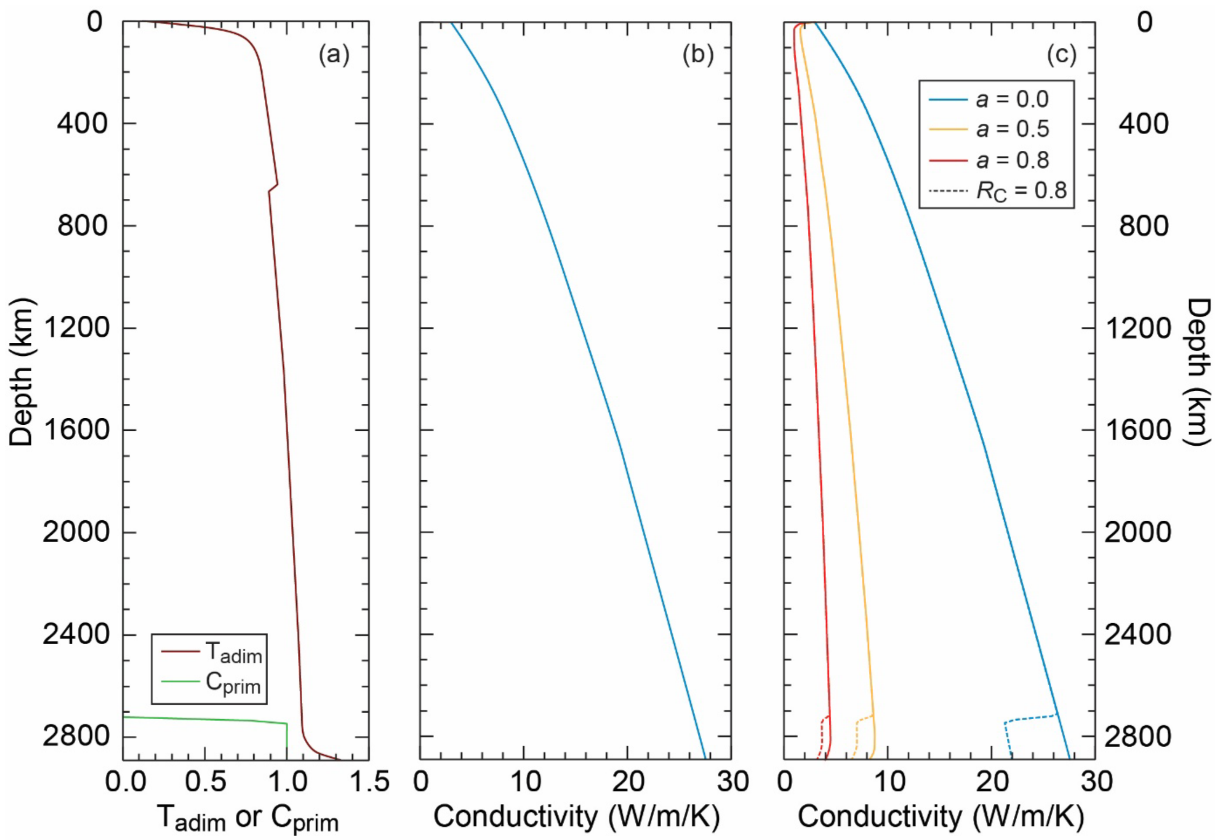

Figure S2. Depth, temperature and compositional dependence of thermal conductivity. Panel (b) shows the intrinsic depth dependence, based on the parameterization of Deschamps and Hsieh (2019). Panel (c) shows the temperature dependence (plain lines) and the combined thermal and compositional dependences (dashed lines) corresponding to the radial models of temperature and composition plotted in panel (a) and for 3 values of the temperature exponent a and (in the case of compositional dependence) R_C = 0.8 (equivalent to a 20 % reduction of conductivity with composition).

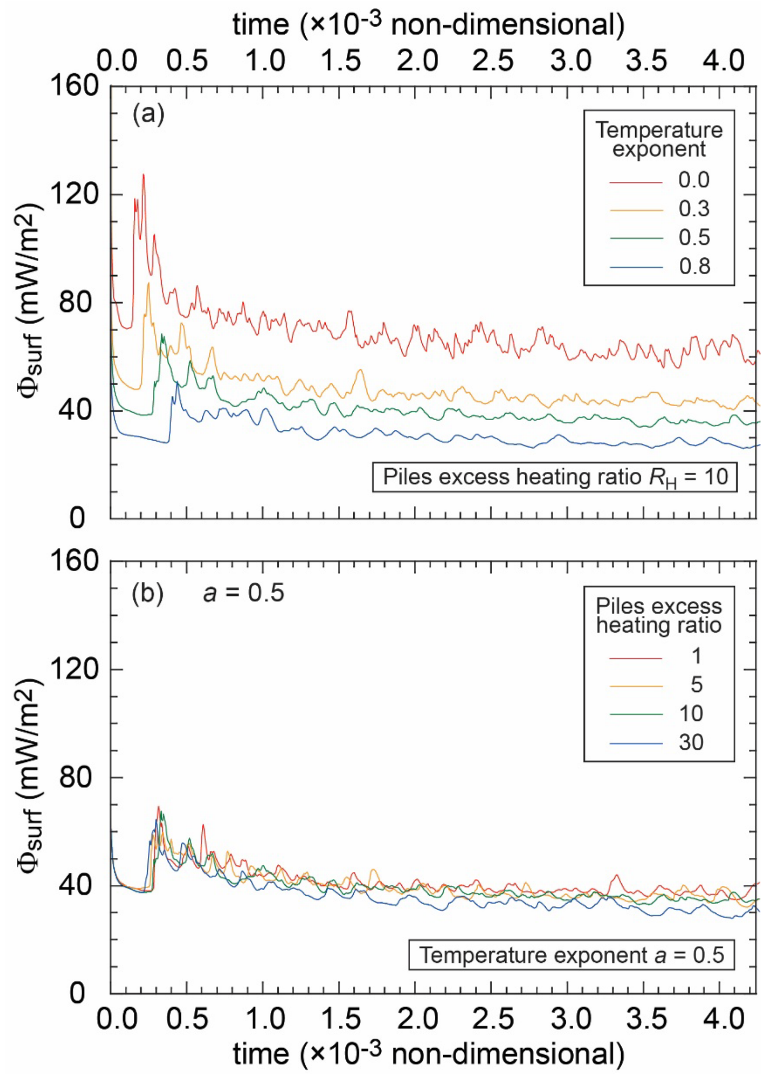

Figure S3. Evolution of the surface heat flux for selected simulations with different temperature-dependence of thermal conductivity, controlled with the temperature exponent *a*, and excess heating ratio in piles of dense material, R_H. In panel (A) R_H is fixed to 10 and 4 values of *a* are considered (see legend). In panel (B), *a* is fixed to 0.5 and 4 values of R_H are considered (see legend).

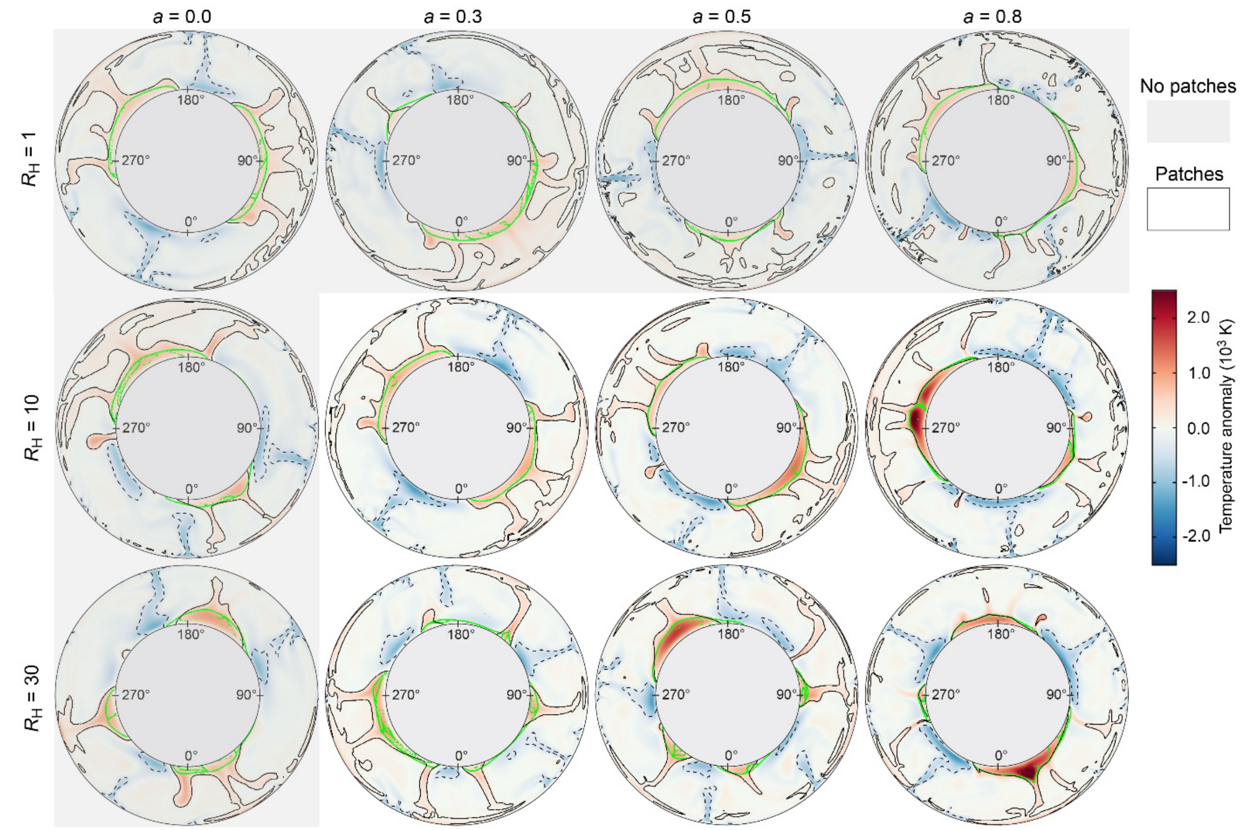

Figure S4. Snapshots of the residual temperature for selected simulations with different temperature-dependence of thermal conductivity, controlled with the temperature exponent *a*, and excess heating ratio in piles of dense material, R_{H}. The plain and dashed black contours represent the boundaries of the plumes and downwelling (as defined in the methods), respectively, and the green contours show the roof of the piles. The gray shaded bands indicate the cases for which we observe patches of negative heat flux at the CMB. Snapshots are taken at the end of each simulation.

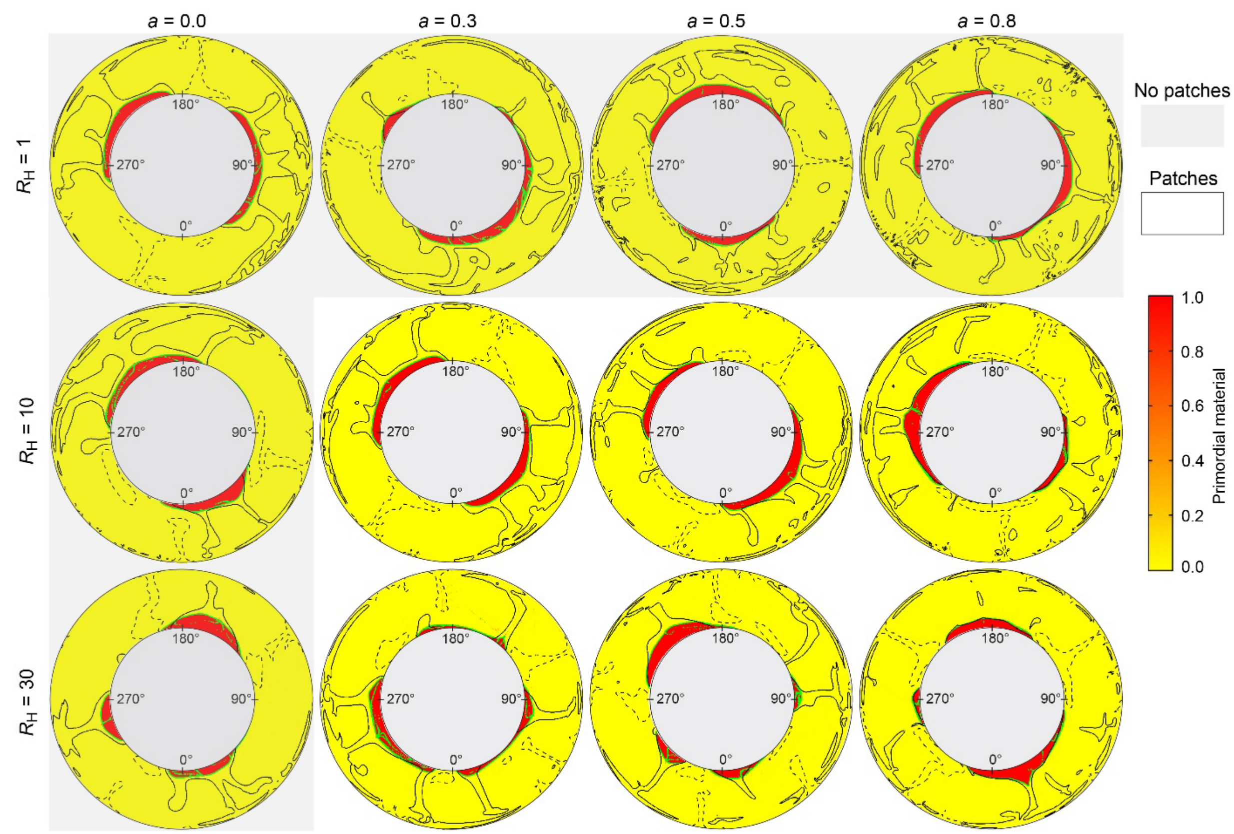

Figure S5. Snapshots of the composition (fraction of primordial material) for selected simulations with different temperature-dependence of thermal conductivity, controlled with the temperature exponent a, and excess heating ratio in piles of dense material, R_H. The plain and dashed black contours represent the boundaries of the plumes and downwelling (as defined methods), respectively, and the green contours show the roof of the piles. The gray shaded bands indicate the cases for which we observe patches of negative heat flux at the CMB. Snapshots are taken at the end of each simulation.

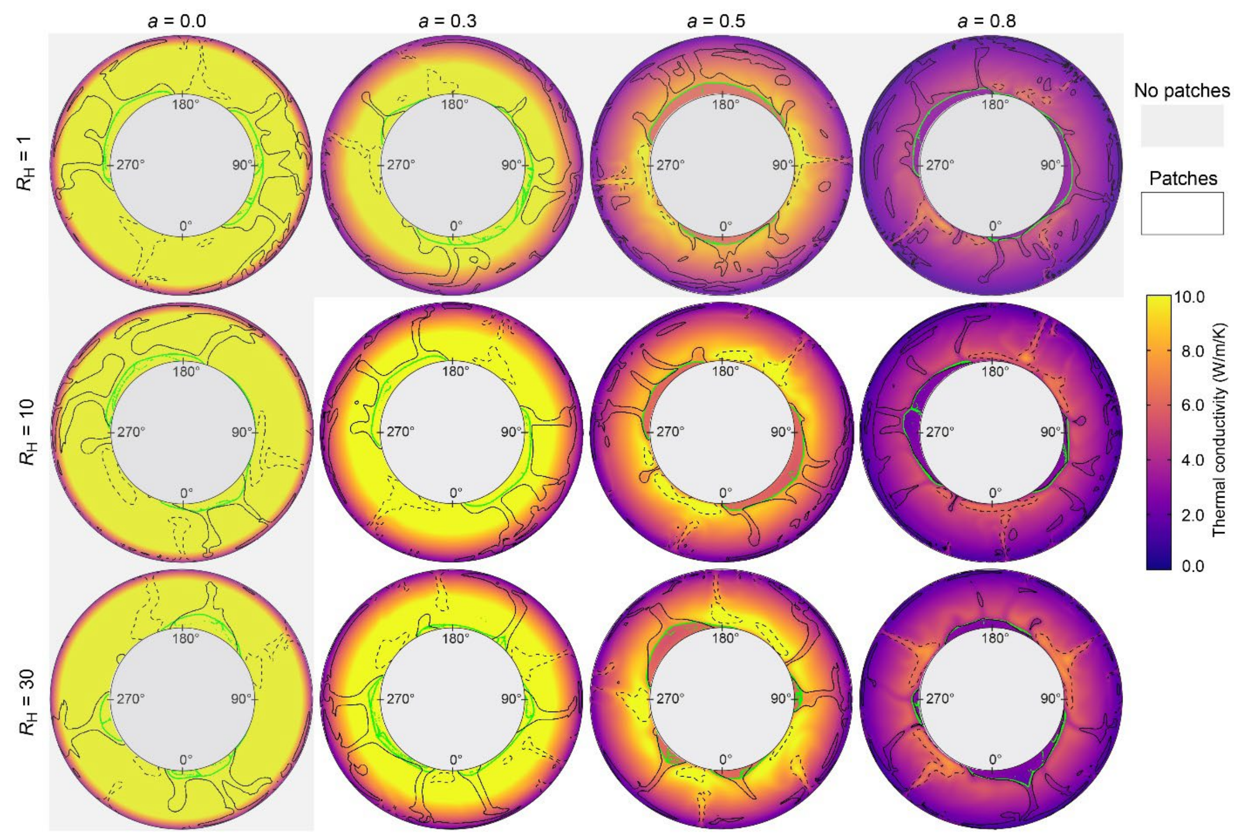

Figure S6. Snapshots of the residual temperature for selected simulations with different temperature-dependence of thermal conductivity, controlled with the temperature exponent a, and excess heating ratio in piles of dense material, R_H. The plain and dashed black contours represent the boundaries of the plumes and downwelling (as defined in methods), respectively, and the green contours show the roof of the piles. The gray shaded bands indicate the cases for which we observe patches of negative heat flux at the CMB. Snapshots are taken at the end of each simulation.

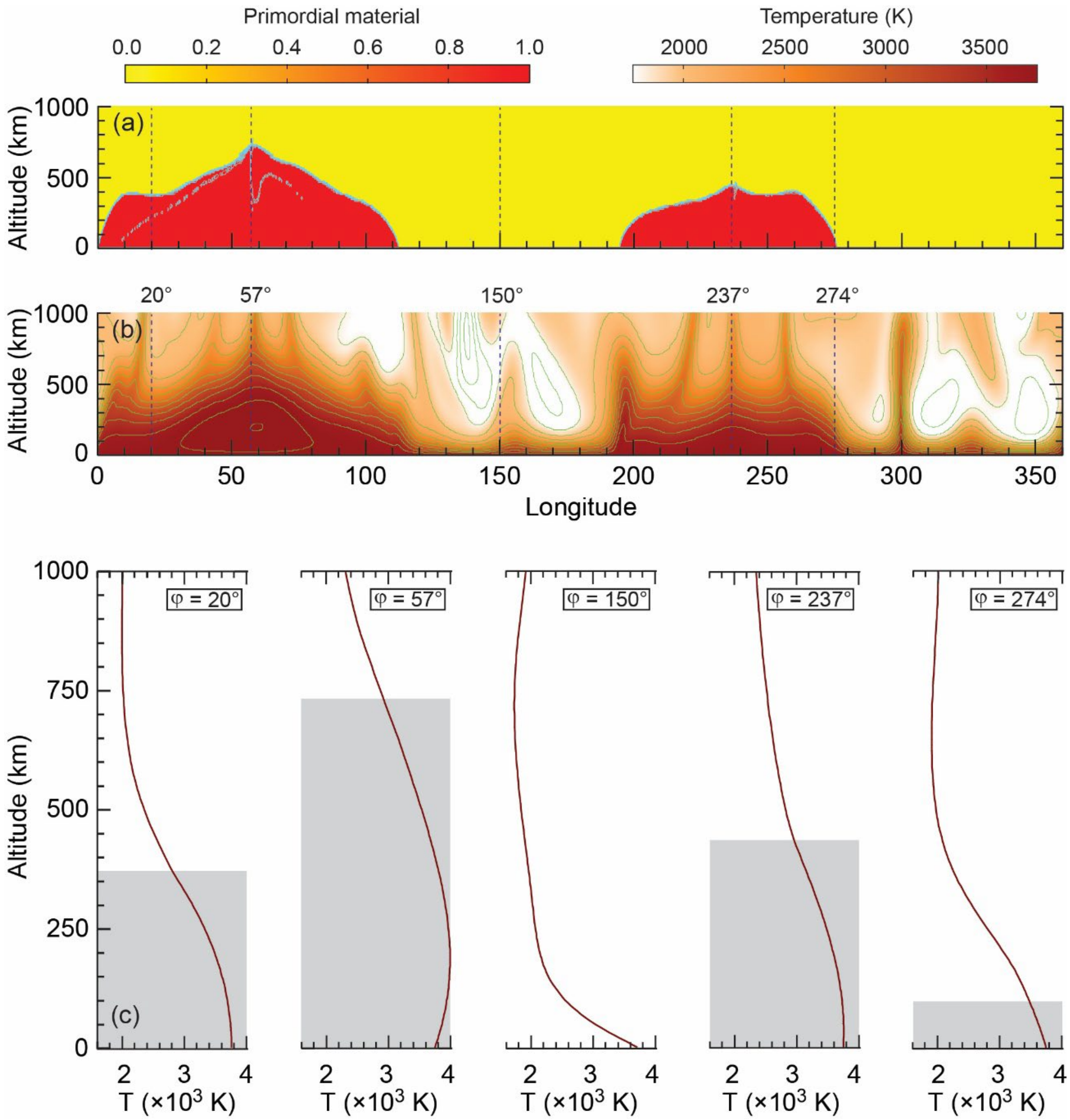

Figure S7. Local radial profiles of the temperature at the bottom of the system. (a) Fraction of primordial material and (b) temperature in the bottom 1000 km. Fields are projected on a 2D-Cartesian grid. In panel (b) the cyan contours indicate composition isolines with an interval of 0.1, and the result from long-term folding of ambient mantle material into piles by the lateral movement caused by downwellings. The (c) Temperature profiles at 5 different locations indicated on plots (a) and (b), including 4 locations sampling the piles of dense material, whose radial extension is here indicated by the grey areas. Note that the temperature profiles are conductive throughout the piles' thickness, implying that piles are not animated by self-convection.

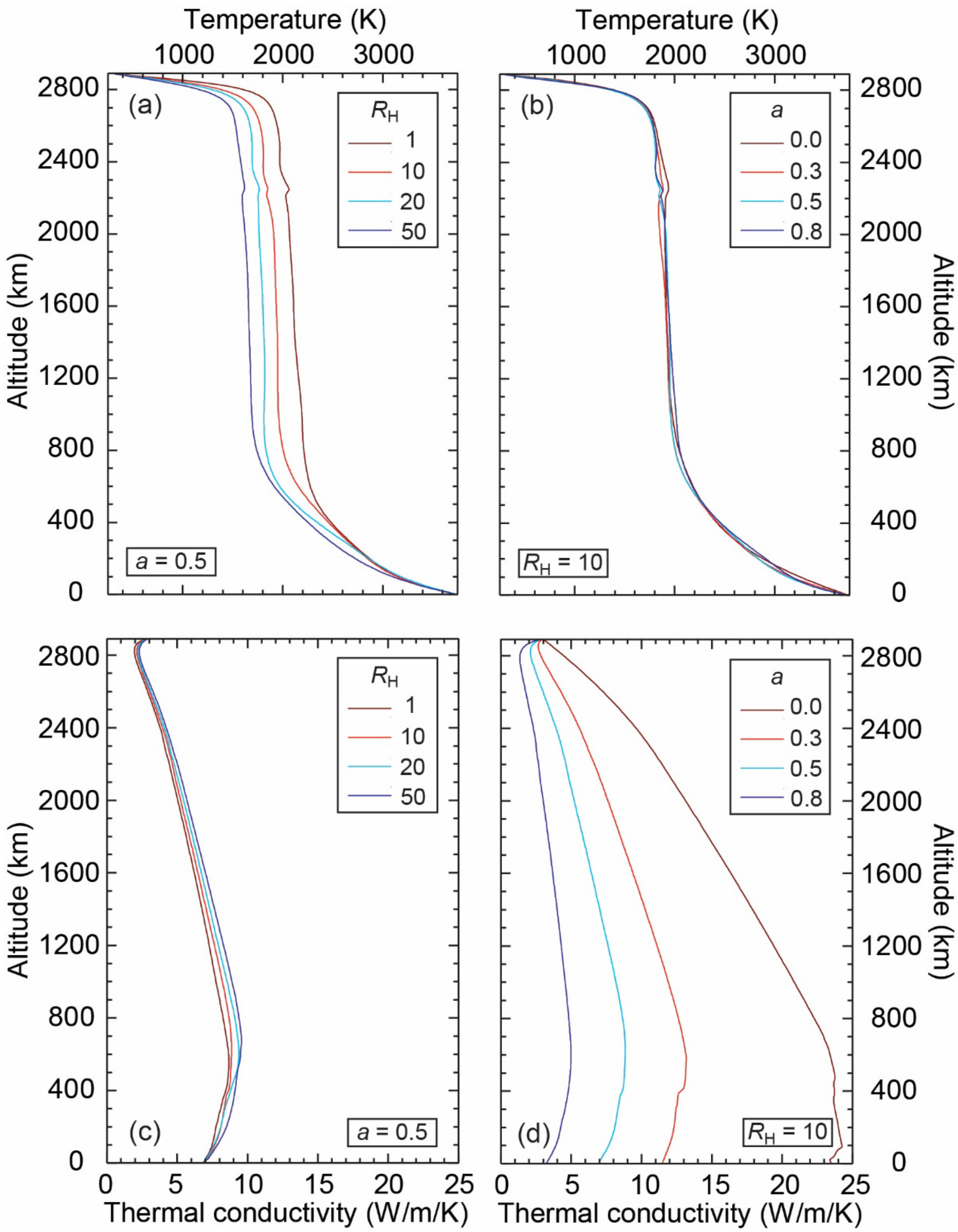

Figure S8. Horizontally average profiles of temperature (a and b) and thermal conductivity (c and d) for selected cases with different thermal conductivity temperature-dependence, controlled with the temperature exponent a, and excess heating ratio in piles of dense material, R_H. In panels (a) and (c), a is fixed to 0.5 and 4 values of R_H are considered (legend). In panels (b) and (d), R_H is fixed to 10 and 4 values of a are considered (legend). All profiles correspond for snapshots taken at the end of each simulation.

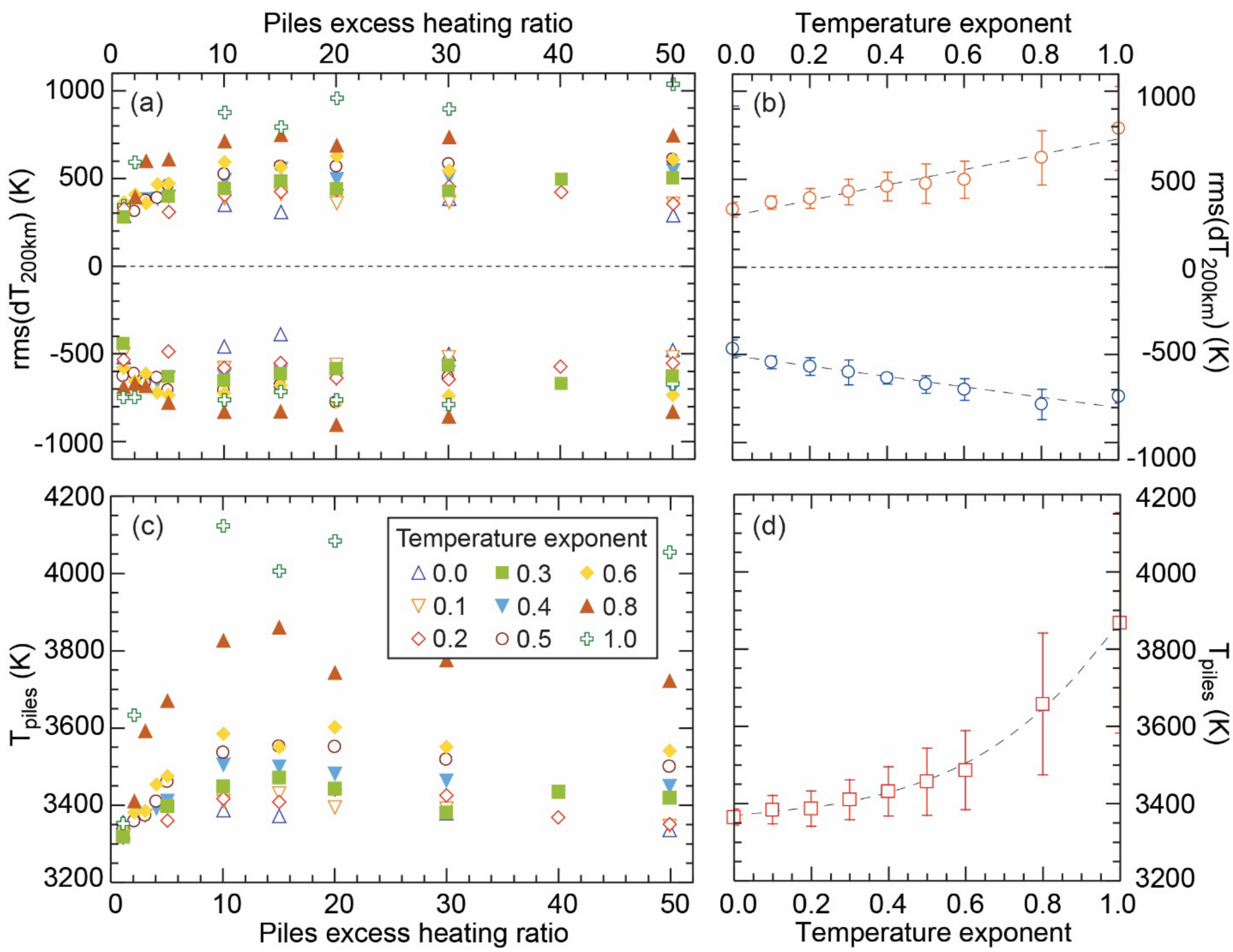

Figure S9. Core-mantle boundary (CMB) temperature statistics averaged over the last 2 Gyr of simulations. (a and b) Root mean square of the positive and negative temperature anomalies in the lowermost 200 km (for convenience, the rms of negative anomalies are multiplied by a minus sign). (c and d) Averages temperature of thermo-chemical piles. Panels (a) and (c) plot data as a function the piles excess heating ratio, R_H, and for several values of the temperature exponent of thermal conductivity, a, (color code). In panels (b) and (d), data are further averaged out over all the values of R_H, the error bars indicating one standard deviation, and represented as a function of the temperature exponent a.

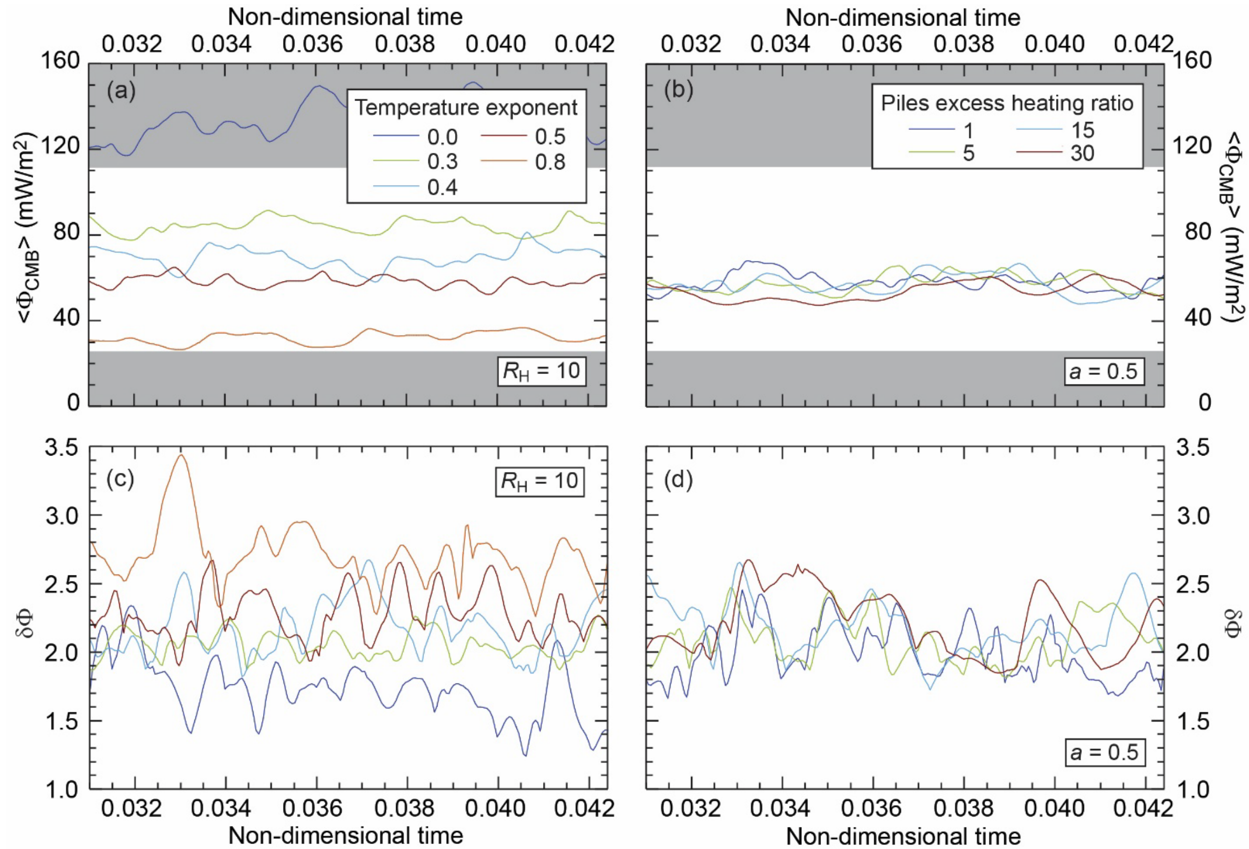

Figure S10. Time variations in (a and b) average CMB heat flux, <Φ_{CMB}>, and (c and d) heat flux heterogeneity δΦ (methods for definition). In panels (a) and (c) the piles excess heating ratio, R_H, is equal to 10 and several values of the temperature exponents of thermal conductivity, *a* (color code), are shown, and in panels (b) and (d) *a* is equal to 0.5 and different values of R_H (color code) are shown. The grey shaded areas in panels (a) and (b) indicate the heat flux values outside the estimate of core power from ref. 36. The time axis is graduated in non-dimensional units, the whole duration being equivalent to 4 Gyr.

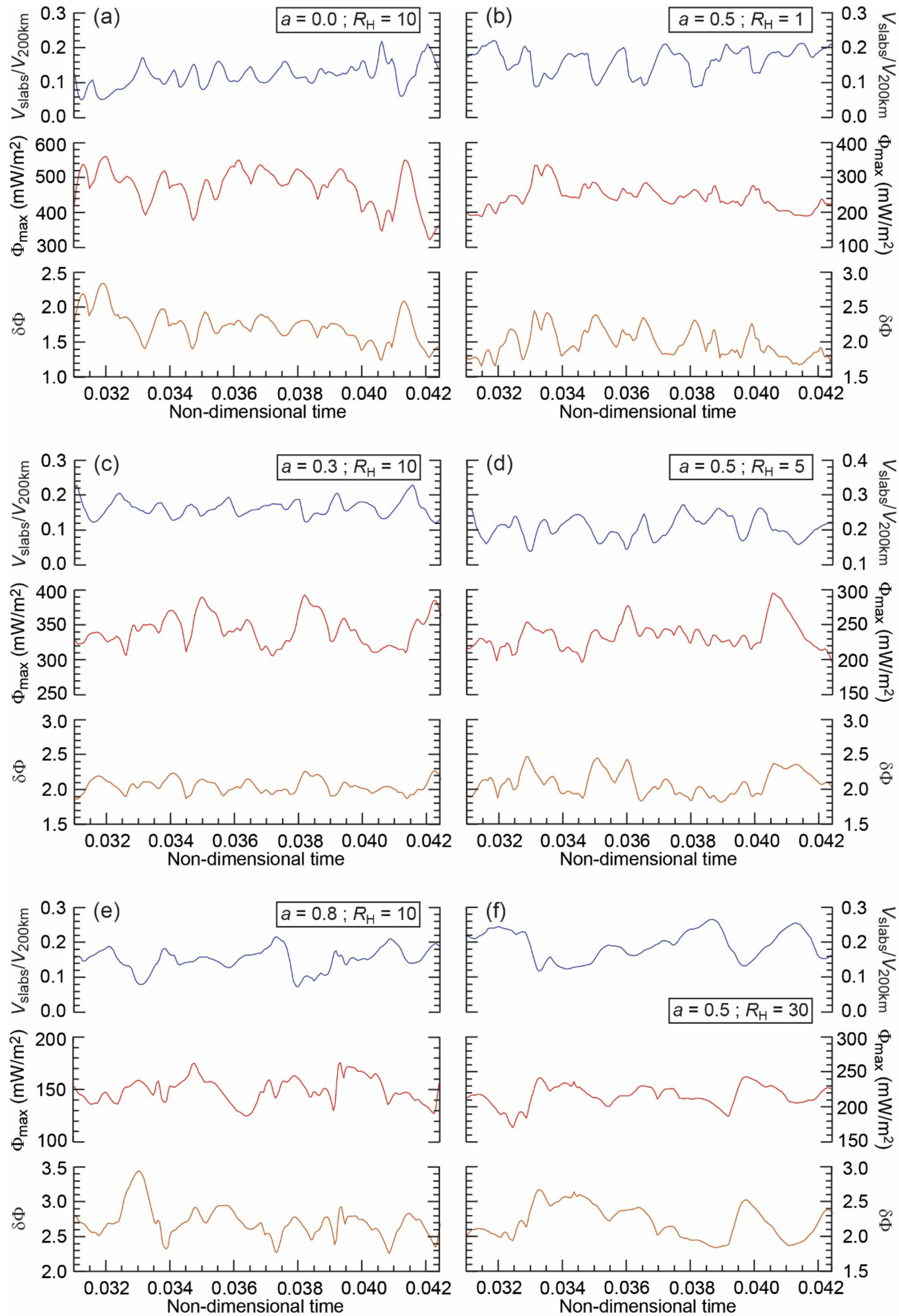
(a)
a = 0.0 ; R_H = 10
(b)
a = 0.5 ; R_H = 1
(c)
a = 0.3 ; R_H = 10
(d)
a = 0.5 ; R_H = 5
(e)
a = 0.8 ; R_H = 10
(f)
a = 0.5 ; R_H = 30
V_slabs/V_200km
Φ_max (mW/m²)
δΦ
Non-dimensional time
0.032
0.034
0.036
0.038
0.040
0.042

Figure S11. Time variations in slab volume fraction in the lowermost 200 km (top row of each panel), maximum CMB heat flux (middle row of each panel), and heat flux heterogeneity (bottom row of each panel) for different combinations of piles excess heating ratio, R_H, and temperature exponents of thermal conductivity, a. The time axis is graduated in non-dimensional units, the whole duration being equivalent to 4 Gyr.

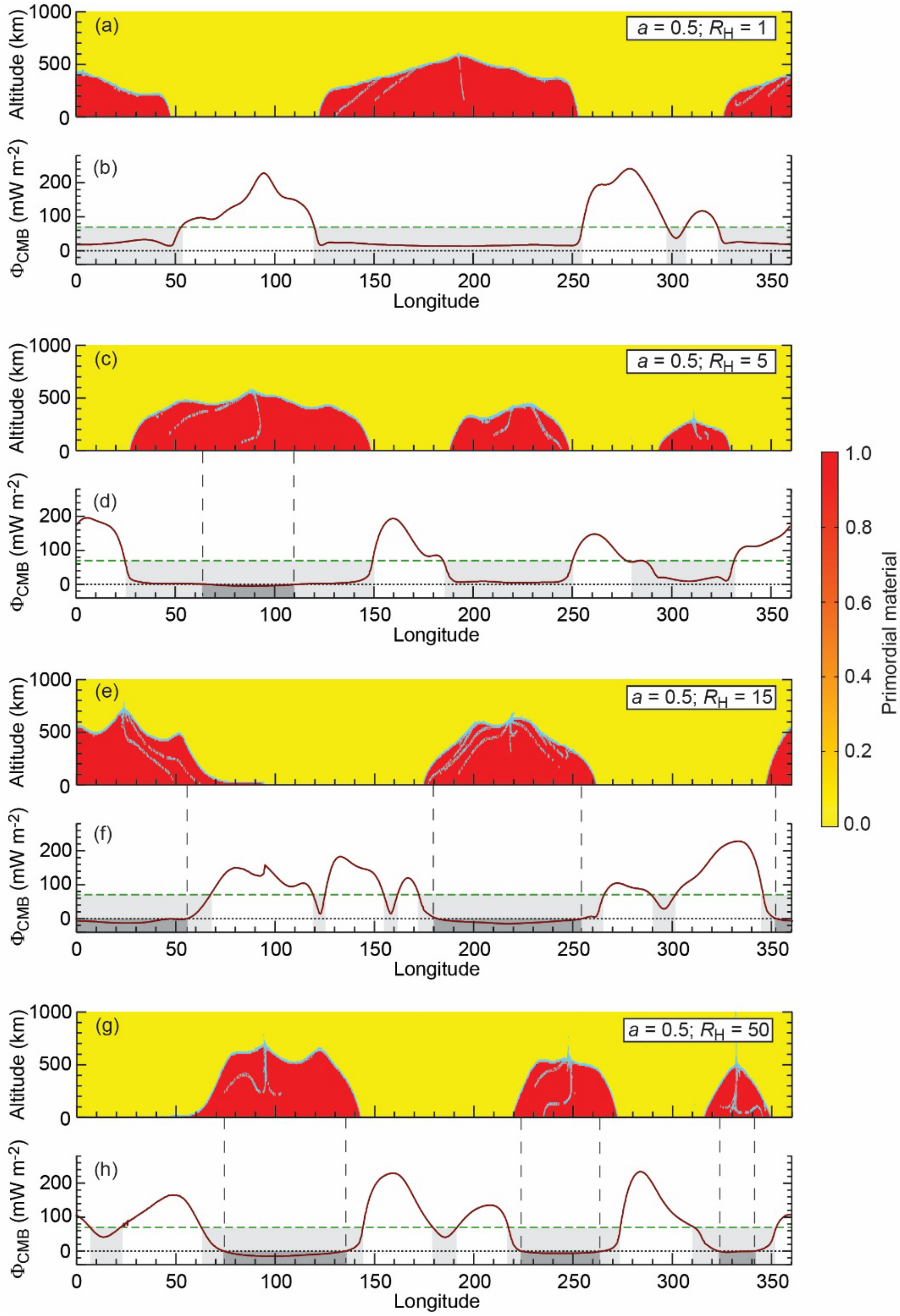

Figure S12. Fraction of dense primordial material, C_{prim} (color code), in the bottom 1000 km, showing piles of dense material, and core-mantle boundary heat flux as a function of longitude for temperature exponent a = 0.5 and several values of the excess piles heating ratio, R_{H}. Data were calculated on a spherical annulus and projected on a 2D-Cartesian grid. In panels showing C_{prim} the cyan contours indicate the composition isolines with an interval of 0.1 In panels showing the CMB heat flux, the green dashed line indicates the core adiabatic heat flux, $\Phi_{\mathrm{adia}}^{\mathrm{core}}$, assuming an adiabatic gradient of 1 K/km and a core conductivity of 70 W m^{-1} K^{-1}, and the light and dark grey areas show the lateral extensions of regions with heat flux lower than $\Phi_{\mathrm{adia}}^{\mathrm{core}}$ and with negative heat flux, respectively.

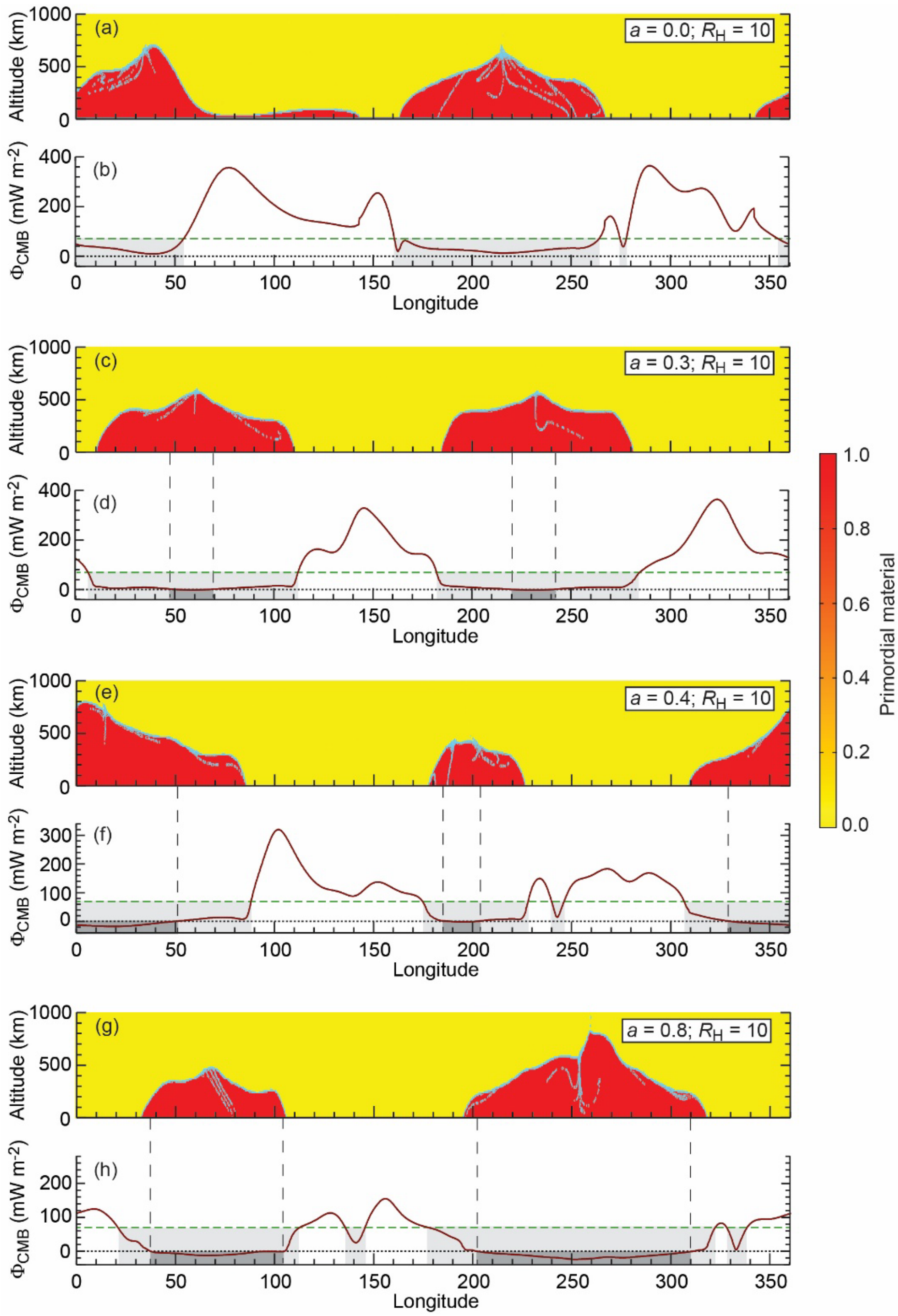

Figure S13. Same as Figure S12, but for an excess piles heating ratio R_H = 10 and several values of the temperature exponent, *a*. Note that in panels showing the CMB heat flux, the scale is different for each plot, as lower values of R_H lead to higher heat flux.

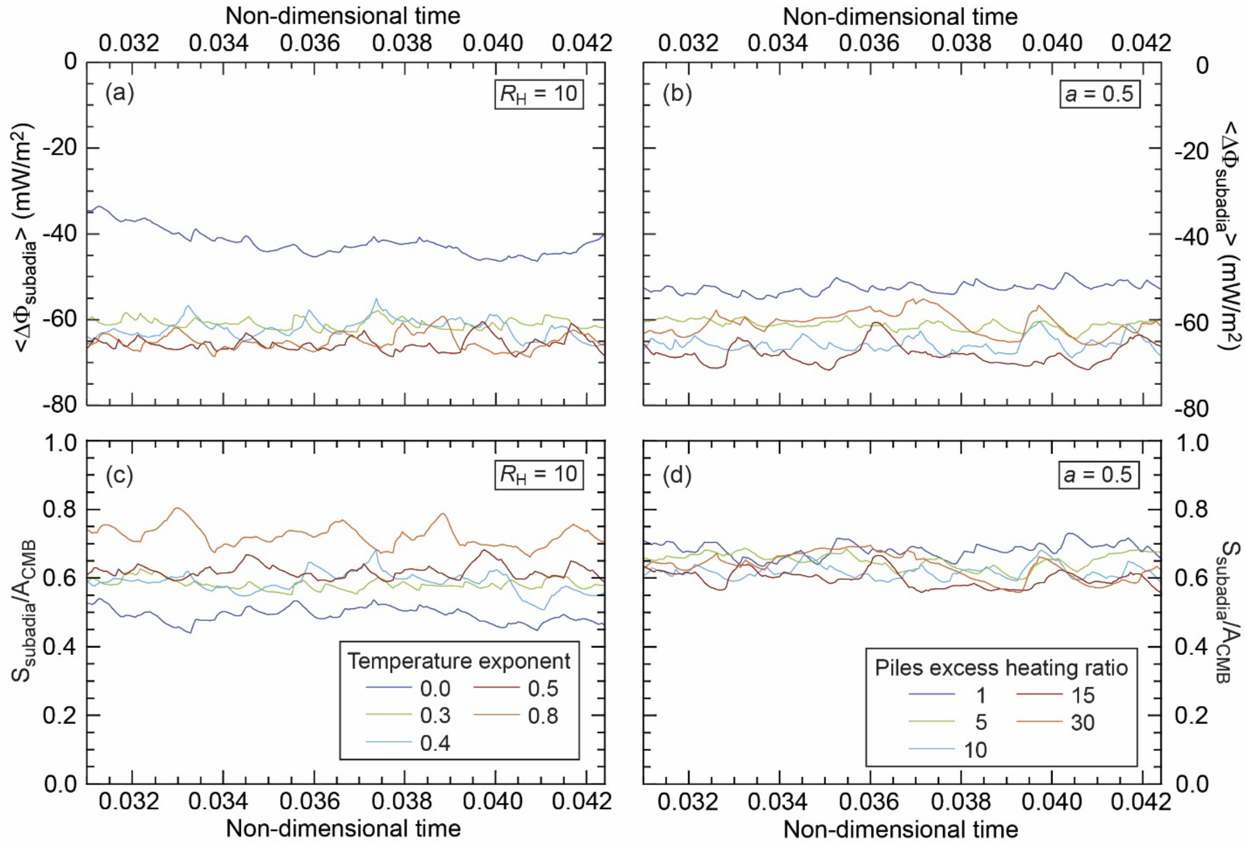

Figure S14. Time variations in (a and b) the average residual subadiabatic heat flux, $<\Delta\Phi_{subadia}>$, defined as the difference between the average heat flux in subadiabatic regions and the core adiabatic heat flux, Φ_{adia}^{core} (here fixed to 70 mW/m^2), and (c and d) the surface fraction (with respect to the CMB area) of the subadiabatic regions. In panels (a) and (c) the piles excess heating ratio, R_H, is equal to 10 and several values of the temperature exponents of thermal conductivity, a (color code), are shown, and in panels (b) and (d) a is equal to 0.5 and different values of R_H (color code) are shown. The time axis is graduated in non-dimensional units, the whole duration being equivalent to 4 Gyr.

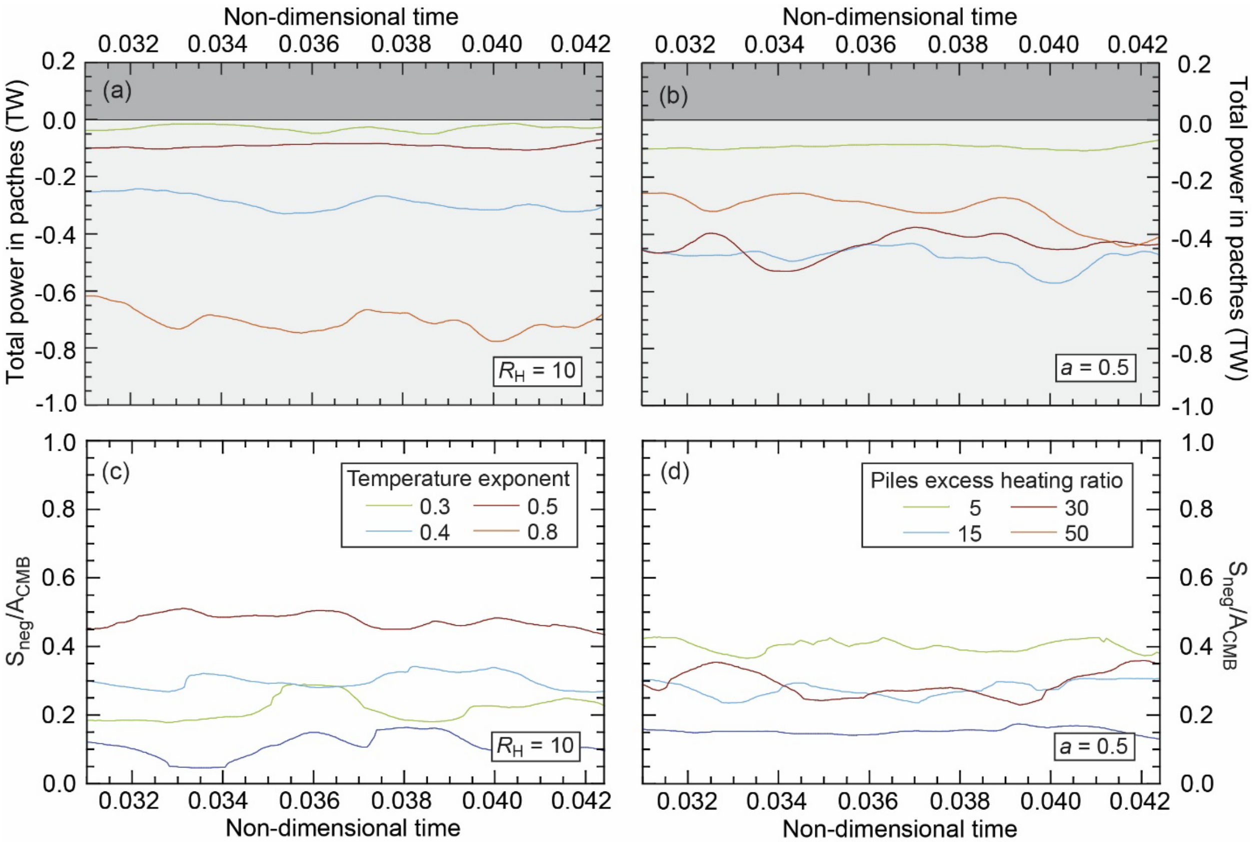

Figure S15. Time variations in (a and b) the total power in patches of negative heat flux, P_{neg}, and (c and d) the surface fraction (with respect to the CMB area) of the negative heat flux regions. In panels (a) and (c) the piles excess heating ratio, R_H, is equal to 10 and several values of the temperature exponents of thermal conductivity, a (color code), are shown, and in panels (b) and (d) a is equal to 0.5 and different values of R_H (color code) are shown. The negative sign in panels (a) and (b) is imposed by convention to indicate that heat flows from the mantle to the core. The time axis is graduated in non-dimensional units, the whole duration being equivalent to 4 Gyr.

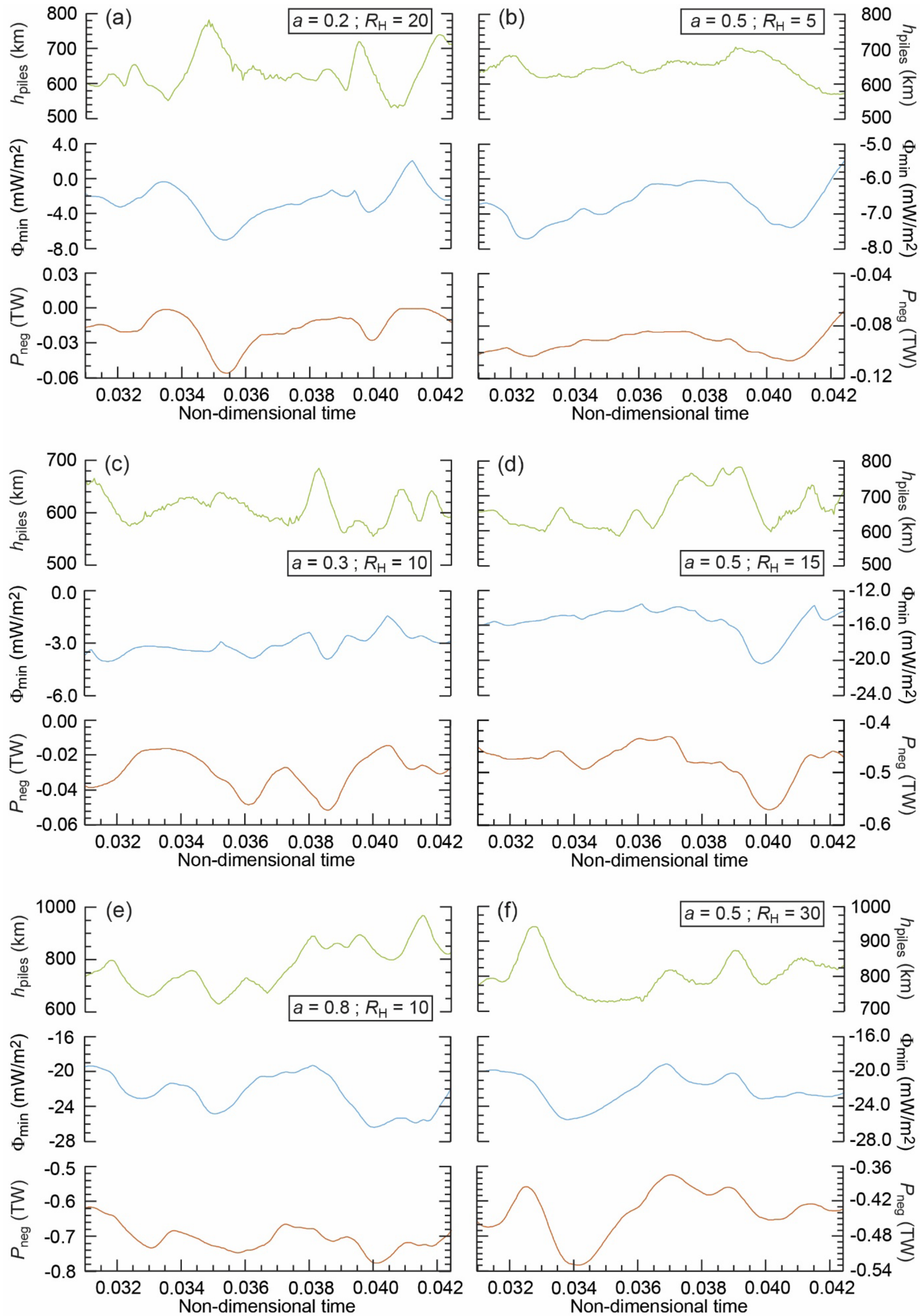
(a)
a = 0.2 ; R_H = 20
(b)
a = 0.5 ; R_H = 5
(c)
a = 0.3 ; R_H = 10
(d)
a = 0.5 ; R_H = 15
(e)
a = 0.8 ; R_H = 10
(f)
a = 0.5 ; R_H = 30
h_piles (km)
Φ_min (mW/m2)
P_neg (TW)
Non-dimensional time
0.032
0.034
0.036
0.038
0.040
0.042

Figure S16. Time variations in piles culminating altitude (top row of each panel), minimum CMB heat flux (middle row of each panel) and total power in patches of negative CMB heat flux (bottom row of each panel) for different combinations of piles excess heating ratio, R_H, and temperature exponents of thermal conductivity, a. The negative sign in the patches power plots is imposed by convention to indicate that heat flows from the mantle to the core. The time axis is graduated in non-dimensional units, the whole duration being equivalent to 4 Gyr.

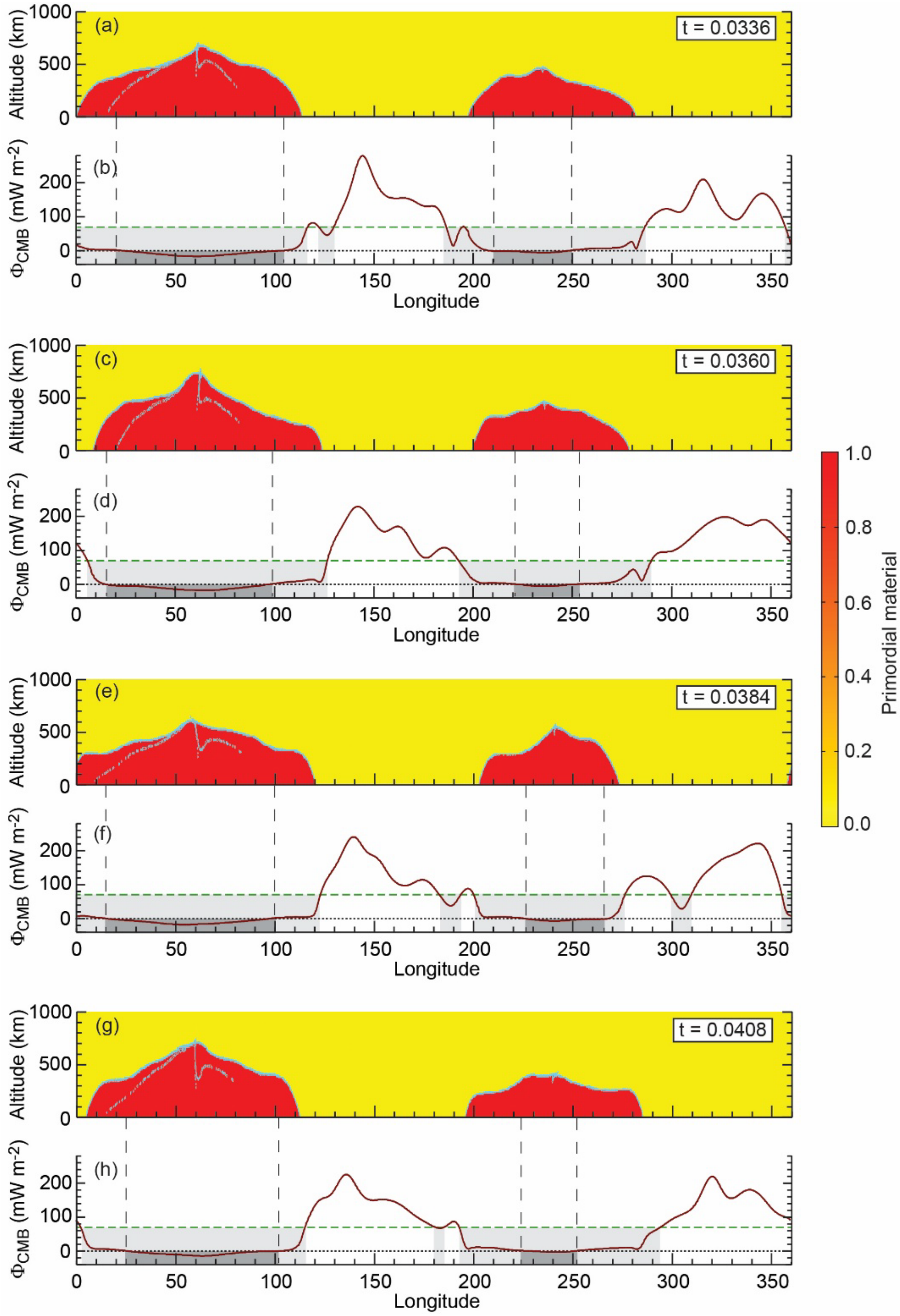

Figure S17. Time sequence of the fraction of dense primordial material, C_{prim} (color code), in the bottom 1000 km, and core-mantle boundary heat flux as a function of longitude for the case a = 0.5 and $R_{\mathrm{H}} = 10$. Data were calculated on a spherical annulus and projected on a 2D-Cartesian grid. In panels showing C_{prim} the cyan contours indicate the composition isolines with an interval of 0.1 In panels showing the CMB heat flux, the green dashed line indicates the core adiabatic heat flux, $\Phi_{\mathrm{adia}}^{\mathrm{core}}$, assuming an adiabatic gradient of 1 K/km and a core conductivity of 70 W m^{-1} K^{-1}, and the light and dark grey areas show the lateral extensions of regions with heat flux lower than $\Phi_{\mathrm{adia}}^{\mathrm{core}}$ and with negative heat flux, respectively.

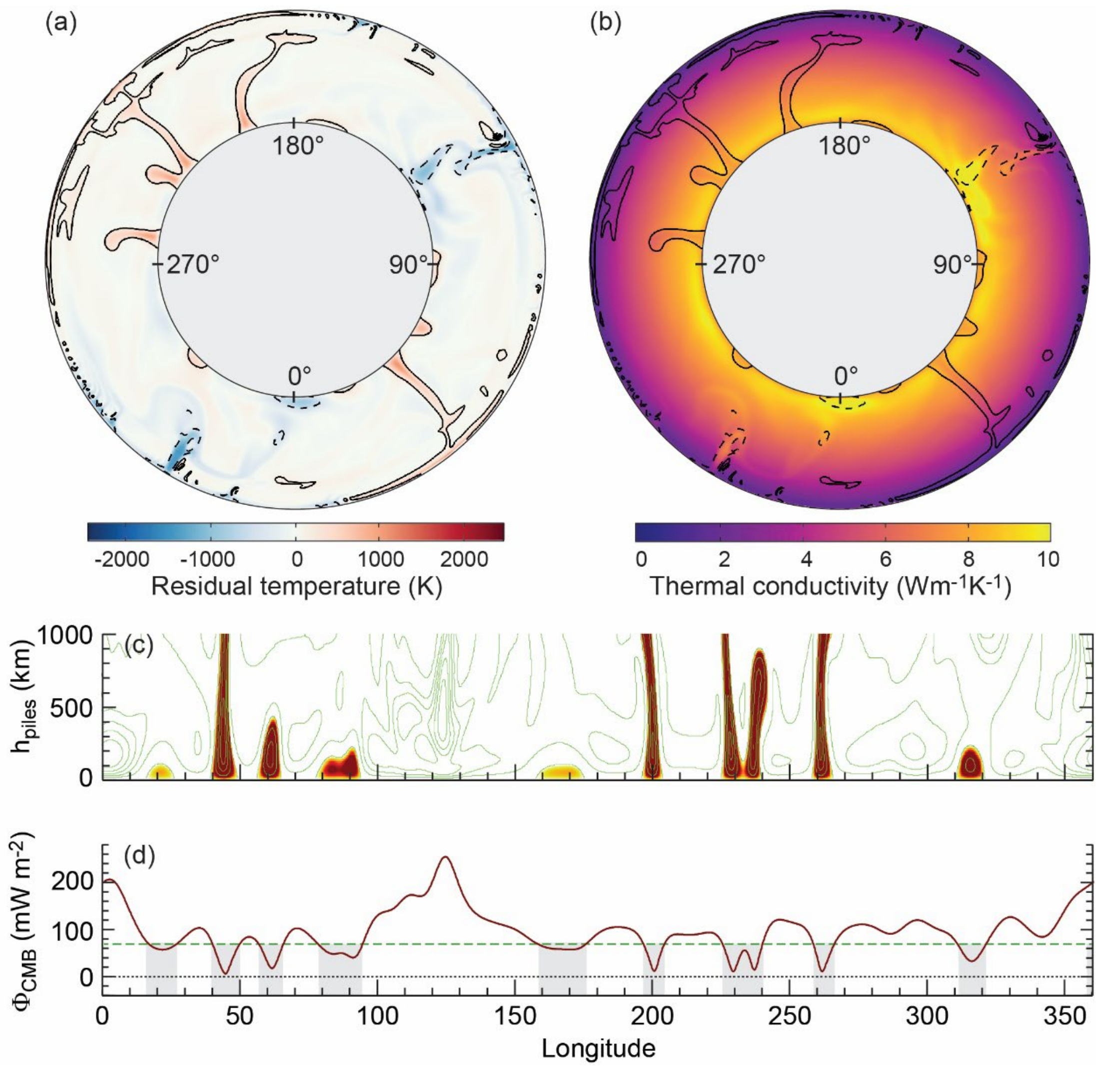

Figure S18. Snapshot of a purely thermal simulation with thermal conductivity temperature exponent $a = 0.5$. (a) Residual temperature. (b) Thermal conductivity. (c) Residual temperature with respect to plumes temperature. (d) core-mantle boundary heat flux as a function of longitude. In panels (a) and (b) the plain and dashed black contours represent the boundaries of plumes and downwelling (as defined in supplementary material), respectively. In panel (c) the spherical annulus is projected on a 2D-Cartesian grid, and the green contours indicate temperature residuals isolines with an interval of 200 K. The color scale goes from white (dT_{plume} = 0 K) to dark red (dT_{plume} = 100 K), and is chosen such that plumes' exterior appear as white and plumes interior as dark red. In panel (d), the green dashed line indicates the core adiabatic heat flux, Φ^{core}_{adia}, assuming an adiabatic gradient of 1 K/km and a core conductivity of 70 W m^{-1} K^{-1}, and the light and dark grey areas show the lateral extensions of regions with heat flux lower than Φ^{core}_{adia} and with negative heat flux, respectively.

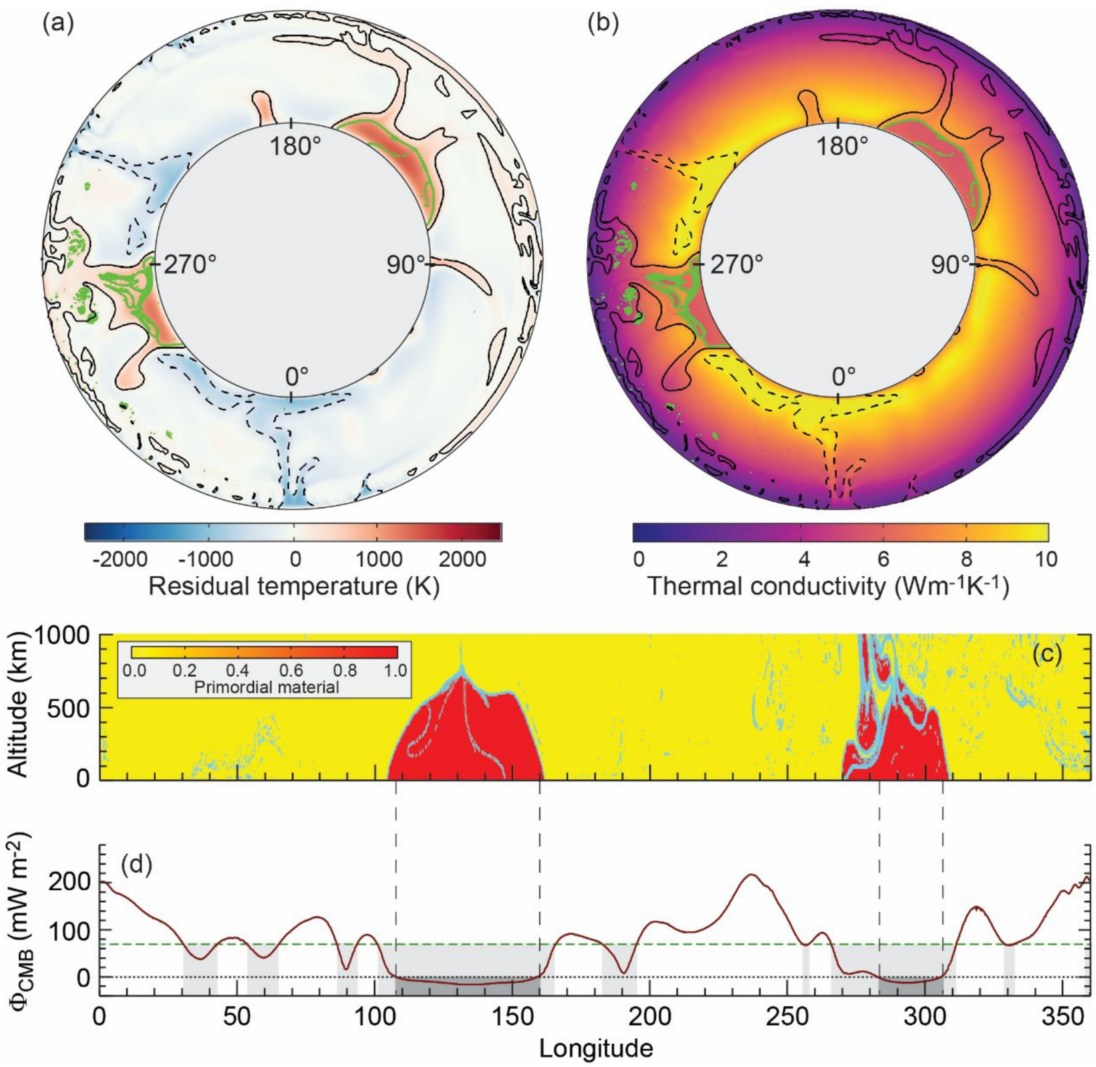

Figure S19. Snapshot of a simulation similar to that shown in Figure 1 ($a = 0.5$ and $R_H = 10$) but but with primordial material density excess of 90 kg/m^3. (a) Residual temperature. (b) Thermal conductivity. (c) Fraction of dense primordial material (color code) in the bottom 1000 km, showing piles of dense material. (d) core-mantle boundary heat flux as a function of longitude. In panels (a) and (b) the plain and dashed black contours represent the boundaries of plumes and downwelling, respectively, and the green contours show the piles roof. In panel (c) the spherical annulus is projected on a 2D-Cartesian grid, and the cyan contours indicate composition isolines with an interval of 0.1. In panel (d), the green dashed line indicates the core adiabatic heat flux, $\Phi_{\mathrm{adia}}^{\mathrm{core}}$, assuming a adiabatic gradient of 1 K/km and a core conductivity of 70 W m^{-1} K^{-1}, and the light and dark grey areas show the lateral extensions of regions with heat flux lower than $\Phi_{\mathrm{adia}}^{\mathrm{core}}$ and with negative heat flux, respectively.

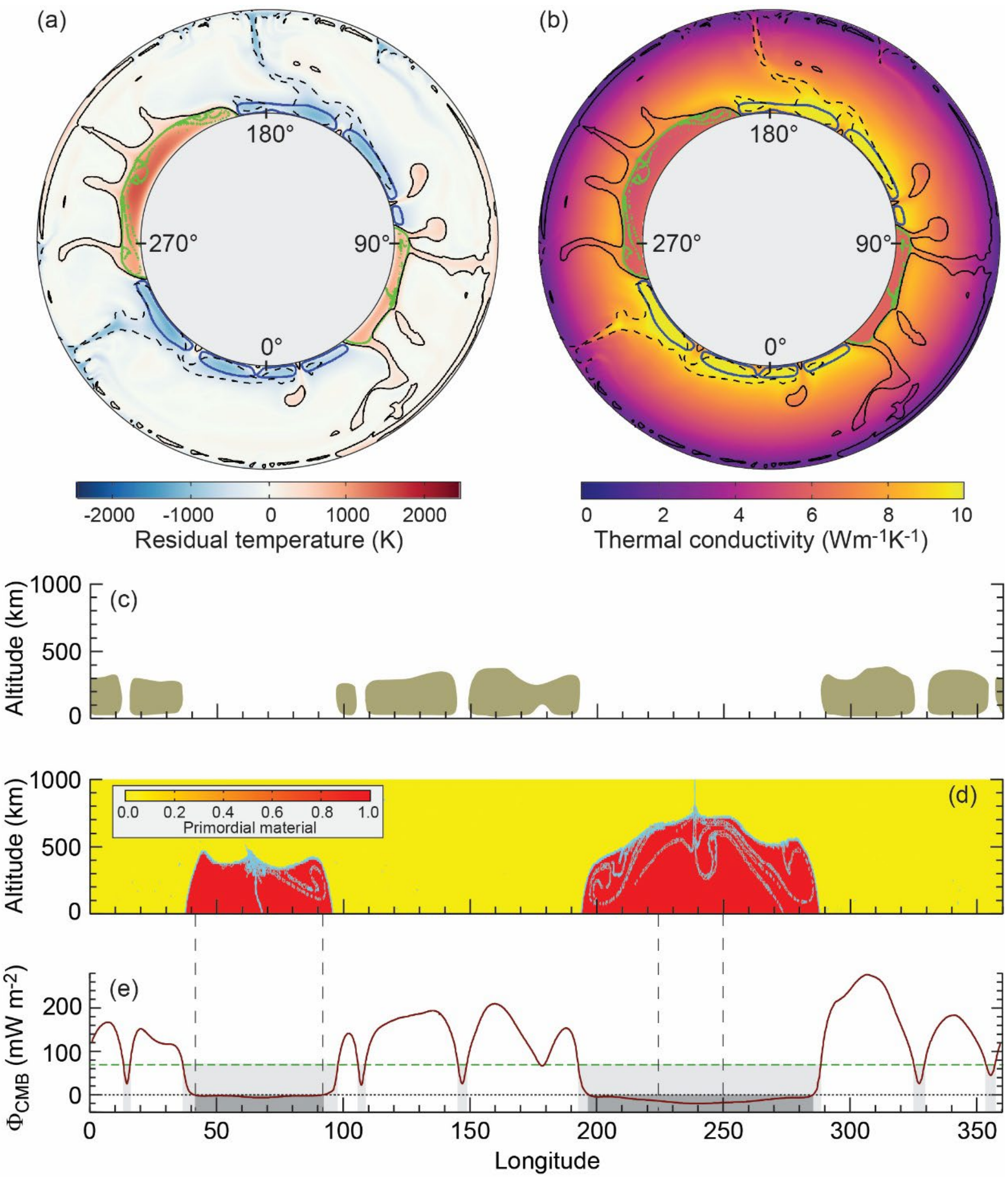

Figure S20. Snapshot of a simulation similar to that in Figure 1 ($a = 0.5$ and $R_H = 10$) and including the post-perovskite (pPv) phase. (a) Residual temperature. (b) Thermal conductivity. (c) Post-perovskite stability field. (d) Fraction of dense primordial material (color code) in the bottom 1000 km, showing piles of dense material. (e) Core-mantle boundary heat flux as a function of longitude. In panels (a) and (b) the plain and dashed black contours represent the boundaries of plumes and downwelling, respectively, the green contours show the piles' roof, and the blue contours the pPv lenses. In panel (c) and (d) the spherical annulus is projected on a 2D-Cartesian grid, and the cyan contours in panel (d) indicate composition isolines with an interval of 0.1. In panel (e), the green dashed line indicates the core adiabatic heat flux, $\Phi^{\mathrm{core}}_{\mathrm{adia}}$, assuming a adiabatic gradient of 1 K/km and a core conductivity of 70 W m^{-1} K^{-1}, and the light and dark grey areas show the lateral extensions of regions with heat flux lower than $\Phi^{\mathrm{core}}_{\mathrm{adia}}$ and with negative heat flux, respectively.

Supplementary movies. Supplementary movies show the evolution show the evolution of the non-dimensional and adiabatic temperature field for 4 cases:

- M01: case HR001, with $a = 0.5$ and $R_H = 10$
- M02: case HR011, with $a = 0.0$ and $R_H = 1$
- M03: case HR009, with $a = 0.8$ and $R_H = 10$
- M04: case HR013, with $a = 0.5$ and $R_H = 30$